11-6-2022

Feedforward control of thermal history in laser powder bed fusion: Toward physics-based optimization of processing parameters

Alex Riensche

Benjamin D. Bevans

Ziyad M. Smoqi

Reza Yavari

Ajay Krishnan

See next page for additional authors

Authors

Alex Riensche, Benjamin D. Bevans, Ziyad M. Smoqi, Reza Yavari, Ajay Krishnan, Josie Gilligan, Nicholas Piercy, Kevin D. Cole, and Prahalada K. Rao
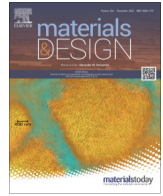
Feedforward control of thermal history in laser powder bed fusion: Toward physics-based optimization of processing parameters

Alex Riensche [a,b,*], Benjamin D. Bevans [a,b], Ziyad Smoqi [b], Reza Yavari [b], Ajay Krishnan [c], Josie Gilligan [d], Nicholas Piercy [b], Kevin Cole [b], Prahalada Rao [a,b]
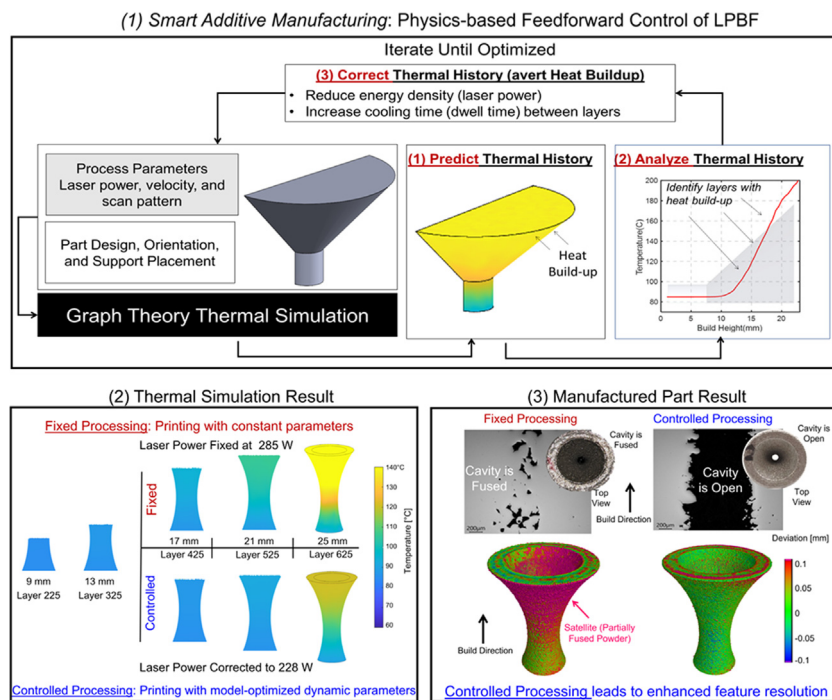
[a] Grado Department of Industrial and Systems Engineering, Virginia Tech, Blacksburg, VA, USA
[b] Mechanical and Materials Engineering, University of Nebraska-Lincoln, Lincoln, NE, USA
[c] Additive Manufacturing, Edison Welding Institute, Columbus, OH, USA
[d] Lincoln High Schools, Lincoln, NE, USA

GRAPHICAL ABSTRACT

ARTICLE INFO

ABSTRACT

We developed and applied a model-driven feedforward control approach to mitigate thermal-induced flaw formation in laser powder bed fusion (LPBF) additive manufacturing process. The key idea was to avert heat buildup in a LPBF part before it is printed by adapting process parameters layer-by-layer based on insights from a physics-based thermal simulation model. The motivation being to replace

⁎ Corresponding author at: Grado Department of Industrial and Systems Engineering, Virginia Tech, Blacksburg, VA, USA.
 E-mail address: ariensche@vt.edu (A. Riensche).

cumbersome empirical build-and-test parameter optimization with a physics-guided strategy. The approach consisted of three steps: prediction, analysis, and correction. First, the temperature distribution of a part was predicted rapidly using a graph theory-based computational thermal model. Second, the model-derived thermal trends were analyzed to isolate layers of potential heat buildup. Third, heat buildup in affected layers was corrected before printing by adjusting process parameters optimized through iterative simulations. The effectiveness of the approach was demonstrated experimentally on two separate build plates. In the first build plate, termed *fixed processing*, ten different nickel alloy 718 parts were produced under constant processing conditions. On a second identical build plate, called *controlled processing,* the laser power and dwell time for each part was adjusted before printing based on thermal simulations to avoid heat buildup. To validate the thermal model predictions, the surface temperature of each part was tracked with a calibrated infrared thermal camera. Post-process the parts were examined with non-destructive and destructive materials characterization techniques. Compared to fixed processing, parts produced under controlled processing showed superior geometric accuracy and resolution, finer grain size, increased microhardness, and reduced surface roughness.

1. Introduction

1.1. Goal and motivation

The goal of this work is to develop and apply a model-driven feedforward control approach for mitigating thermal-induced flaw formation in metal parts made using laser powder bed fusion (LPBF) process. In this work, temperature predictions from a physics-based computational simulation model are used to adjust the processing parameters layer-by-layer before the part is printed with the intent of avoiding heat buildup and subsequently reducing thermal-induced flaw formation. The motivation is to replace cumbersome and expensive build-and-test empirical optimization with a physics-guided strategy.

In LPBF, as shown in Fig. 1(left), metal powder is raked or rolled onto a build plate and selectively melted layer-by-layer using energy from a laser [1]. Despite its demonstrated potential to reduce lead time and overcome design-related constraints, LPBF has yet to displace conventional manufacturing, particularly in precision-driven industries, owing to its tendency to create flaws, which eventually leads to large variability in functional properties [2-5].

The spatiotemporal temperature distribution in the part during the LPBF process, also called the thermal history, is reported to be the major cause of such flaw formation scenarios as sub-standard geometric integrity; poor surface finish; build failures, e.g., recoater crashes and collapse of supports; cracking and distortion; inconsistent microstructure, among others [2,3,6-9].

Recently, Sames *et al.* [7] provided a comprehensive review of research efforts linking thermal history to flaw formation and physical properties of LPBF parts. For example, Li *et al.* [10] associated heat buildup with grain coarsening, which in turn results in reduced microhardness. Likewise, Paulson *et al.* [11] established the effect of heat buildup in single track deposits on keyhole porosity. Similarly, Yavari *et al.* [9,25] correlated excessive heat buildup in samples to part warpage leading to recoater crashes, microstructure heterogeneity, and porosity. Therefore understanding, predicting, and controlling the thermal history is essential to ensure industrial-scale viability of the LPBF process [12].

The thermal history of LPBF parts is influenced by several factors such as: processing parameters; part design; part orientation, layout and build plan; other parts on the build plate; and feedstock materials aspects [7,8]. Moreover, the thermal history of a part may vary substantially from layer-to-layer due to the changing surface area of the part [9]. Hence, thermal-induced flaw formation can occur despite using empirically optimized processing conditions.

The causal effect of thermal history on part quality is illustrated in Fig. 1(right), which shows a LPBF build plate consisting of seven identical stainless steel parts printed under manufacturer-optimized processing conditions. The parts differ only in their orientation and were made under the same processing conditions that remained constant throughout the build. Out of the seven parts printed, only two were observed to be nominally flaw-free, the rest of the five parts were afflicted with thermal-induced flaws, such as cracking and warping.
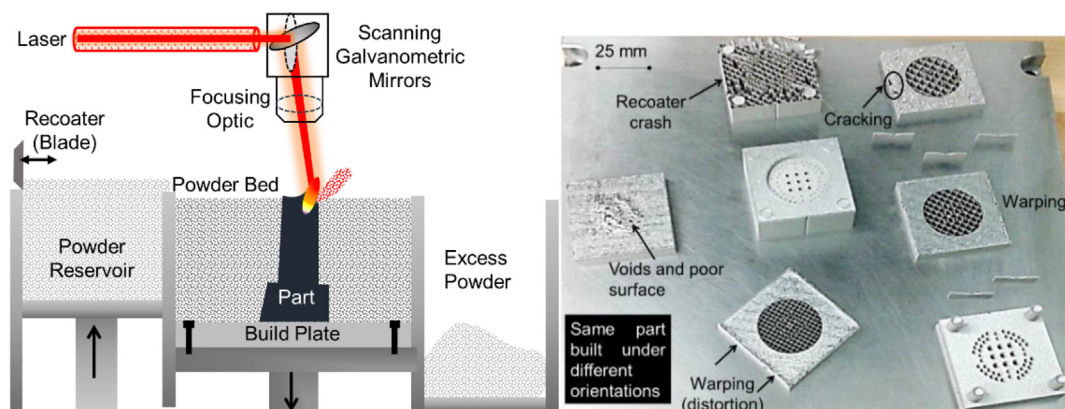
Fig. 1. (Left) Schematic of the laser powder bed fusion (LPBF) metal additive manufacturing process (Right) The LPBF process is prone to flaw formation despite extensive empirical optimization of processing parameters. For example, the same part when built under identical parameters in different orientations results in various types of flaws, such as warping, cracking, poor surface finish, and recoater crash.

The flaws exemplified in Fig. 1(right) can be attributed to the existing empirical approach to process optimization. In current LPBF practice, simple cuboid or cylinder-shaped coupons are deposited under different processing conditions (e.g., laser power, velocity, hatch spacing, scan pattern). Subsequently, the test coupons are examined post-process, typically with non-destructive X-ray computed tomography and destructive metallographic analysis [13-15]. Based on these empirical tests, practitioners identify optimal processing parameters for obtaining a desired physical characteristic, such as porosity, part density, surface finish, or mechanical property, e.g., tensile strength [16,17].

While specific flaws, such as porosity, may be prevented with optimized processing conditions, other types of non-conformities such as distortion and inconsistent microstructure often occur in intricate parts due to underlying complex process physics, part design and orientation interactions [18]. Therefore once processing parameters are optimized for a particular material, experienced practitioners further adapt these parameters for making complex geometries [6].

Such subjective geometry-specific, build-and-test empirical optimization is expensive and laborious given there are over 50 critical-to-quality LPBF process variables, prohibitive cost of powder feedstock materials, and small production batch sizes [19]. Consequently, there is an urgent need to supplant empirical process parameter optimization with a physics-guided predictive strategy that encompasses the causal relationship between parameters, part design, thermal history and part quality [12,20-22].

1.2. Objective and approach

1.2.1. Concept of model-based feedforward control

The objective of this work is to demonstrate that model-driven feedforward process control mitigates thermal-induced flaw formation in LPBF parts. The key idea of feedforward control implemented in this work is to avert heat buildup in an LPBF part by optimizing the process parameters layer-by-layer before printing based on insight from a computational thermal simulation model. The approach consists of three steps, as summarized in Fig. 2.

(Step 1) _Predict_ the thermal history (temperature distribution) of a LPBF part using a fast and computationally tractable graph theory approach [9,23,24].

(Step 2) _Analyze_ the predicted thermal history trends and identify layers where excessive heat buildup is likely to occur. The control target is the rate of change, or slope, of end-of-cycle surface temperature. The end-of-cycle temperature is the surface temperature of the part after a layer is deposited and a fresh layer of powder is placed above, but prior to melting of the next layer. The goal is to maintain the slope at 0 °C per layer. Control is only initiated when the rate of change of end-of-cycle temperature exceeds 20 °C per layer.

The threshold of 20 °C per layer was determined based on our previous work detailed in Ref. [9,25] for identical material and LPBF system. In these previous studies an increase in end-of-cycle surface temperature greater than 20 °C between successive layers was correlated with build failures, such as distortion and recoater crashes [9].

(Step 3) _Correct_ heat buildup in layers identified in Step 2 by adjusting the laser power layer-by-layer or by increasing the dwell time between layers, thus allowing the part to cool. These processing conditions are optimized through iterative simulation of the thermal history using the graph theory approach.

The prediction of thermal history and changes to process parameters are guided by a experimentally validated graph theory thermal simulation approach detailed in prior publications [9,23,25-28]. This mesh-free computational thermal modeling approach converges approximately 7 to 10 times faster than existing non-commercial finite element-based LPBF simulations on a desktop PC, and the thermal history is predicted with error less than 10% [9,23,25-28].

The computational advantage of the graph theory approach allows practitioners to rapidly iterate and simulate the effect of changing processing conditions on the thermal history before a part is printed. Thus, this model-driven feedforward control strategy can significantly reduce the need for extensive empirical opti-

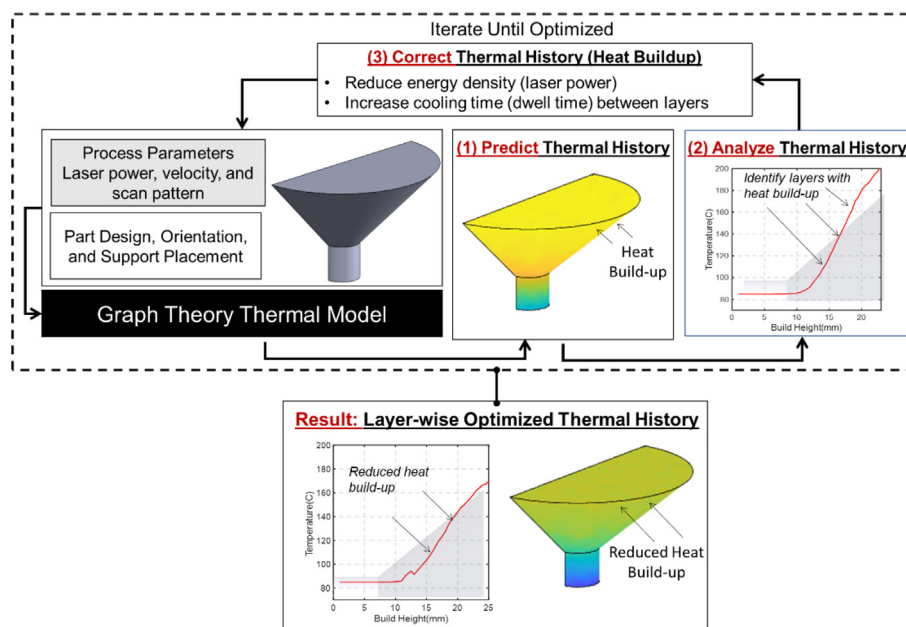**Fig. 2.** This model-driven feed forward control of additive manufacturing approach consists of three steps. (Step 1) Prediction of thermal history using the graph theory computation model. (Step 2) Analysis of the predicted thermal history trends to identify heat buildup. (Step 3) Correction of heat buildup by adjusting process parameters layer-by-layer optimized through iterative simulation of the thermal history.

mization and testing to mitigate flaw formation, and thereby accelerate the time-to-market of LPBF parts.

To demonstrate the effectiveness of the feedforward approach two identical build plates were used. Each build plate consisted of 16 parts encompassing 10 types of geometries parts made from Nickel Alloy 718 material. In the first build plate - *fixed processing* - all parts are printed under identical, powder manufacturer-recommended processing parameters, and these parameters are maintained constant throughout the process for all layers of the part. In the literature, fixed processing is also referred to as traditional processing [29].

The second build plate - *controlled processing* - has identical parts printed under matching conditions except the laser power was changed layer-wise depending on the geometry of each part, and the dwell time between layers was increased to mitigate heat buildup. Preventing heat buildup was the target of the feedforward control approach presented in this work due to its correlation with flaw formation The parameter changes for the controlled processing case are optimized *a priori* through thermal simulations. Each part on the controlled processing build plate is printed with a unique, build strategy aimed at minimizing heat buildup specific to the part geometry. For the parts in this work, the graph theory-based thermal simulations converged in between 2 and 10 minutes on a desktop PC.

Post-process the physical properties of parts built under fixed and controlled processing conditions are compared using a variety of ex-situ non-destructive and destructive characterization techniques. Specifically, non-destructive X-ray computed tomography was used for measurement of porosity, surface texture and geometric accuracy. The Archimedes method was used for relative density measurements. Destructive metallography characterization involved optical and scanning electron microscopy, and measurement of microhardness.

1.2.2. Limitations

A limitation with the feedforward control approach developed in this work stems from the objective of mitigating heat buildup at the bulk part-scale. Controlling the heat buildup at the part-scale was successful at reducing various types of scale-transcending flaw formation, such as microstructure grain size, surface finish, and geometric accuracy. However, an alternative, and more focused approach, would be to target scale-specific outcomes, e.g., type and texture of microstructure evolved, residual stresses, and feature resolution, among others. These could be achieved by controlling certain thermal phenomena, such as cooling rate and spatial thermal gradients. A second drawback of the presented approach is that heat buildup in the part is mitigated between layers, and not within a layer due to limited resolution of the graph theory model.

Further, in this work, the adjustment of process parameters are identified through trial-and-error iterative simulation of the thermal history trends from the graph theory model. The mitigation of heat buildup is achieved by adjusting only two process parameters in the model, namely, laser power and dwell time between layers. In other words, the control design is heuristic and based on observation. In our future work, the process parameter adjustment will be automated through purpose-built optimization algorithms with a broader scope of control variables.

1.3. Prior work and novelty

A brief literature review concerning process control for LPBF is provided herewith. Review articles detailing process control strategies are available in Ref. [30-33]. As summarized in Fig. 3, approaches for process control in LPBF can be categorized into two broad classes – closed-loop feedback control, and open-loop feedforward control.

1.3.1. Review of prior work in Closed-loop feedback control in LPBF

In closed-loop control, the process dynamics, e.g., meltpool temperature or part temperature, are observed using a sensor, such as a pyrometer or thermal camera, and process drifts are corrected based on data acquired from the sensor [29,34-36]. For example, Renken *et al.* [37], installed a pyrometer in the LPBF machine to measure the intensity of the meltpool during processing. Subsequently, a data-driven control algorithm was used to maintain the meltpool intensity within a tight window by adjusting the laser power. The control schema described above falls under the category of empirical sensor-based closed-loop control, since the correction strategy was not guided by a physics-based model.

In the same work, Renken *et al.* [37] implemented a hybrid empirical and physics-guided closed-loop control strategy wherein a finite element (FE) model is used to guide the process corrections. In other words, the meltpool intensity tracked by the pyrometer is used as an input to an FE model which, in turn, determines the control action, i.e., reduce or increase laser power. Renken *et al.* [37] report, based on experiments with bridge-shaped parts (similar to one of the parts studied in this work, see Table 2, Sec. 2.2.1), that the hybrid feedback control approach outperforms sensor-based feedback control, in that the meltpool temperature has a smaller deviation when processing certain overhang features of the part.

Recently, Vasileska *et al.*[38] successfully demonstrated a feedback control approach based on real-time imaging of the meltpool in LPBF. The aim was to control the meltpool shape and size by changing the duty cycle of a pulsed laser, which in turn resulted in improved feature resolution of overhang bridge-shaped parts.

From a bulk part temperature perspective, Zhong *et al.* [29] developed a neural network machine learning-based feedback mechanism for controlling the thermal history in LPBF parts. The inputs to the neural network were surface temperature images from a thermal camera and certain derived process signatures. Similar to this work, the aim was to minimize heat buildup in the part by altering the laser power layer-by-layer. Zhong *et al.* [29] demonstrated the utility of the feedback control approach in the context of tensile test specimens and a large (1 m × 1.65 m) LPBF part. The authors reported that the feedback control mechanism reduced the variation in tensile strength across coupons to within 10%, compared to over 30% for fixed processing. Notably, Zhong *et al.*'s [29] work was carried out on a quad-laser LPBF system, and the material used was resin-coated sand.

There are two challenges in applying closed-loop feedback control strategies to LPBF. First, there is an inherent delay in the sensing and feedback loop which can potentially hinder early detection and correction of process drifts. Second, sensors for temperature measurement in LPBF, such as imaging pyrometers or thermal cameras, only provide surface temperature information and cannot capture the temperature distribution of the entire part beyond the top layer.

1.3.2. Review of prior work in open-loop feedforward control in LPBF

In the open-loop feedforward control category, the process state is not adjusted online based on feedback from a sensor. Instead, changes are made to the process parameters before printing to compensate for predicted process deviations based on model-derived predictions [39-47]. Feedforward control is, therefore, proactive in nature. These feedforward process models can be empirically derived [39-41], physics-based [42-44,46], or a hybrid of physics and empirically derived models [45]. This work is an example of open-loop feedforward control with process parameter optimization executed offline via a physics-based model before the part is built.
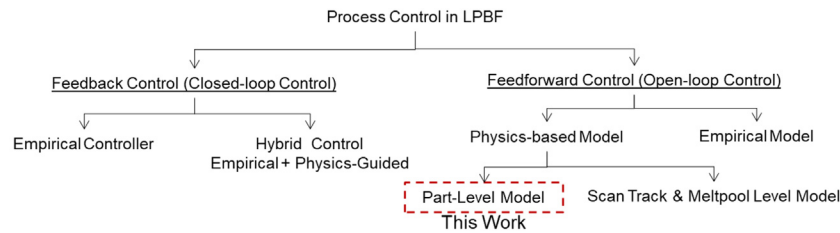
Fig. 3. There are two approaches for process control in LPBF implemented in the literature. (left) closed-loop feedback control, and (right) open-loop feedforward control. The present work employs part-level model-based feedforward control.

As an example of empirical feedforward control in LPBF, Heung *et al.* [40] used a shape-related factor called the geometric correction factor (GCF) to reduce the laser power when scanning a part with overhang regions. As a consequence, Hueng *et al.* [40] demonstrated that the overhang regions are not overheated, which resulted in improved surface finish [40]. A drawback with such an empirical feedforward control strategy is that the model is restricted to certain shapes and features representative of the available data, i.e., application of the GCF to other features beyond overhangs, such as thin walls, remains to be investigated.

From the perspective of model-driven feedforward control, a physics-based computational or analytical model is used to adjust the process parameters. In the literature, feedforward control based on physical thermal models both at the bulk part-level [44] and track-level have been implemented [46]. Further, approaches that couple high-fidelity simulations with a low-resolution empirical model have also been proposed [47].

To reduce the computational burden involved with physics-guided feedforward control, researchers often employ a simplified abstraction of a high-fidelity model. For example, Ramani *et al.* [46] used radial basis functions to approximate the heat transfer simulations at the scan-level obtained from a finite difference model. Based on one-layer thick scans of area 600 mm × 600 mm, Ramani *et al.* [46] show that a scanning pattern derived from their model-based approach (termed *SmartScan*) significantly reduced distortion compared to conventional, empirically derived strategies, such as chessboard and rectilinear scanning patterns.

Druzgalski *et al.* [44] optimized the laser power and velocity settings at the hatch-level using a physics-based model. For this purpose, Druzgalski *et al.* [44] leveraged the ALE3D FE code developed by Lawrence Livermore National Laboratory [48]. Hatch-level thermal simulations were used to prevent heat buildup within a layer by changing the laser scanning parameters in a heuristic manner. To demonstrate the effectiveness of their approach, Druzgalski *et al.* built a complex geometry with internal channels and overhang features with fixed conditions, and their model-optimized layer scan strategy. Through post-process characterization, Druzgalski *et al.* [44] demonstrated that compared to fixed processing, model-optimized processing resulted in parts with superior resolution and improved surface integrity.

Our work differs from Druzgalski *et al.*'s approach in one consequential aspect. Druzgalski *et al.*'s approach relies on high-resolution hatch-level FE simulation to optimize the laser parameters within a layer. Instead of hatch-level temperature control, the current work is concerned with avoiding heat buildup at the overall bulk part-level by adjusting the laser power and dwell time between layers. A rapid and relatively low-resolution graph theory approach is used in this work for predicting the heat buildup. Moreover, the current work demonstrates the advantages of feedforward control in the context of four different part shapes with post-process measurements ranging from quantification of microstructure in terms of grain size, surface finish, dimensional integrity, and microhardness.

A data and model-driven hybrid feedforward process control strategy is implemented in the work of Ogoke *et al.* [45], who use an empirical machine learning model (deep reinforcement learning) to optimally adjust the process parameters at the hatch- or track-level. The machine learning model is user trained from theoretical finite element simulations. Recently, Wang *et al.* [43] used an analytical model to predict and control the meltpool depth for avoiding keyhole and lack-of-fusion porosity in LPBF.

In closing this section, we note that a hybrid feedforward and feedback control of the LPBF process is being studied as part of our future work. The concept is to augment sensor-based feedback control to correct local within layer heat buildup based on data from an in-line sensor, with model-based feedforward control to mitigate between layer heat buildup.

1.3.3. Novelty

This work has two unique aspects that differentiate it from the existing model-based feedforward process control approaches reported in the literature. First, previous work in the literature employed computationally demanding part-scale FE-based thermal simulation models that require several hours to converge, this work uses a mesh-free graph theory model that converges within minutes (<15 min) on a desktop PC [9,49,50]. Although commercial FE-based solutions for thermal modeling can drastically reduce the computation time, they do not currently incorporate the ability to automatically prescribe adjustment of parameters to compensate for potential heat buildup and related process drifts [51]. However, we note that certain commercial solutions (ANSYS Additive Print) do provide the ability to modify the part design to compensate for thermal-induced distortion [51].

Second, current efforts in feedforward control in LPBF are largely restricted to single track and meltpool-scale process control, with a few focusing on part-scale thermal modeling [43-46]. The presented approach is scalable to a variety of relatively complex and large, multi-layer parts. Within this context, the thermal model and effect of feedforward control are validated through in-situ thermography measurements.

1.4. Organization of the paper

The rest of this paper is organized as follows. In Sec. 2, we describe the experimental methodology and graph theory simulation approach. Results are reported in Sec. 3 which includes model validation, and comparison of physical properties, such as part resolution, surface finish, microstructure, and microhardness for multiple parts built with and without model-based feedforward control. Finally, the conclusions and avenues for future research are summarized in Sec. 4.

2. Methodology

This section is organized as follows. Sec. 2.1 details the experimental LPBF setup. Sec. 2.2 reports the build plan and provides the

rationale for choosing the various test parts studied in this work, as well as details the post-processing steps used for characterization of part properties. Sec. 2.3 explains the procedure for measurement and calibration of the in-process temperature measurements obtained from the thermal camera. Finally, Sec. 2.4 elucidates the graph theory-based feedforward process control approach implemented in this work.

2.1. Experimental setup

Parts were manufactured using the open architecture LPBF system at Edison Welding Institute (EWI, Ohio). A schematic and picture of the sensor instrumented LPBF system is presented in Fig. 4 (a) and (b) respectively; its specifications are provided in Table 1. This LPBF system allows critical processing parameters, such as laser power, dwell time between layers, scan path, and laser velocity among others to be independently altered, layer-by-layer, for each part on the build plate.

The system is equipped with a SCANLABS HurryScan20 galvanometer-mirror scanner, a 700 W 1062 nm Yb-fiber laser (IPG Photonics YLR – 700WC) and a precision motion control system (Aerotech A3200) driven by CNC G-code that can be edited by an operator. The system produces a nominal spot size of 68 μm at 370 W – measured by a laser beam profiling system (Ophir BeamWatchAM).

A Micro-Epsilon model με thermoIMAGE TIM 640 longwave infrared (LWIR) thermal camera with an operating wavelength of 8 to 14 μm is installed inside the machine chamber. The camera is inclined at 80° to the horizontal and acquired data at 10 Hz. The optical resolution of the camera is 640 pixels × 480 pixels. The camera settings are also summarized in Table 1. The thermal camera was positioned to capture an approximately 125 mm × 125 mm central area of the build plate resulting in a spatial resolution ∼20 pixels per mm². The camera was triggered by a G-code command before the laser began scanning a layer and was stopped after the laser completed that layer. Hence, data was only acquired when the laser was actively melting material.

As will be detailed in Sec. 2.3.1, the IR camera measurements are calibrated offline using an industry-standard approach to absolute temperature with reference contact thermocouple readings. Recently, Wang, *et al.* [52] developed a similar approach to measure the top surface temperature using infrared thermography.

Table 1
Nominal process parameter settings and material properties. Also included are the settings used for the IR thermal camera.

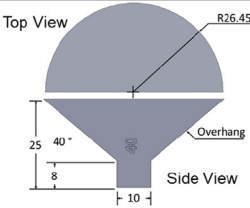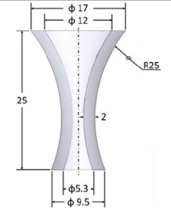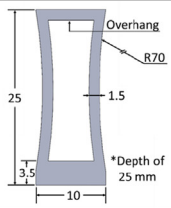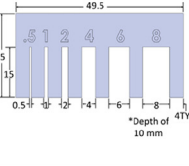| Process Parameter [Units]	Values
Laser type and wavelength.	Ytterbium fiber, wavelength 1070 nm continuous mode (manufacturer IPG), 700 W max power
Nominal Laser Power (P_0) [W]	285
Scanning Speed (V) [mm s^{-1}]	960
Hatch spacing (H) [mm]	0.1
Layer thickness (T) [mm]	0.04
Stripes overlap [mm]	0.08
Stripe width [mm]	10
Volumetric global energy density E_v [W/mm³]	73
Laser spot size [μm]	68
Scanning strategy	Meander-type scanning strategy with 45° rotation of scan path between layers.
Build atmosphere	Argon
Build plate Preheat temperature [°C]	85
Recoater Cycle Time [sec]	15
Powder Material Properties	Values [units]
Material type	Nickel Alloy 718 (Ni718); corresponding to UNS N07718 (Carpenter Additive)
Particle size range [μm]	15–45 (D10 – D90)
IR Thermal Camera Specifications	Values
Brand and model	Micro Epsilon – thermoIMAGER TIM 640
Resolution [pixels], [pixel per mm²]	640 × 480, 20
Frame rate [Hz]	10
Spectral range [μm]	8 to 14
Spatial resolution of object in image [μm/pixel]	20
Camera On trigger event	Laser Start
Image size [mm]	125 × 125

Additionally, a Hall effect current sensor is connected to the recoater to capture the recoater motion. This sensor provides an estimate of the recoating time and detects load on the recoater blade, which is valuable for detecting recoater impact. The time for recoating a layer with fresh powder is measured to be 15 seconds and remained fixed irrespective of the process conditions or
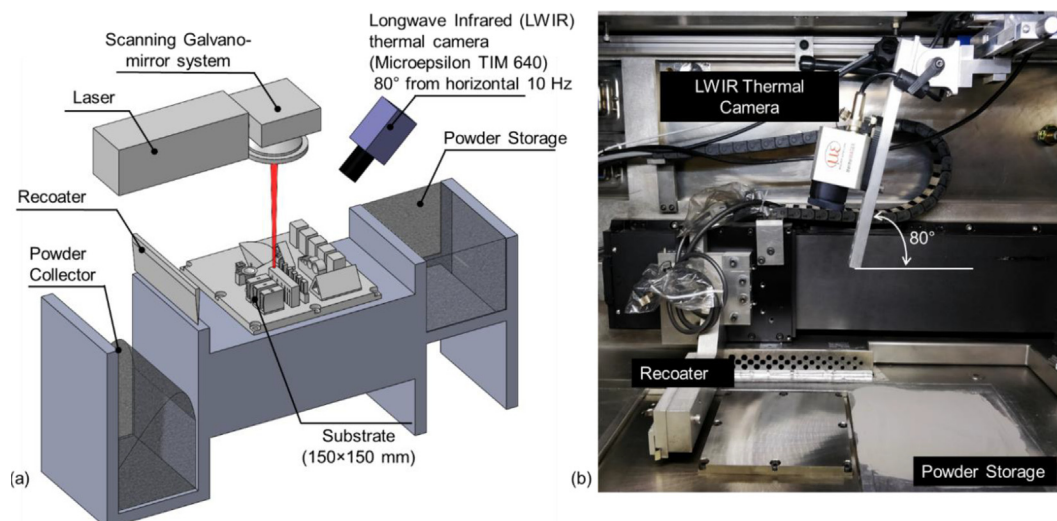
Fig. 4. (a) Schematic, and (b) photograph of the open architecture LPBF system at Edison Welding Institute (EWI). An infrared thermal camera inclined at 80° to the horizontal was installed in the chamber to monitor the surface temperature of the parts during processing.

Table 2
The four parts selected for analysis, their underlying rationale, and post-process characterization.

	Cone	Vase	Frame	Bridge
Part Geometry	Top View R26.45; 25 40° 8 10 Side View; Overhang	φ17 φ12 R25 25 2 φ5.3 φ9.5	Overhang R70 25 1.5 3,5 10 *Depth of 25 mm	49.5 .5 1 2 4 6 8 25 15 0.5 1 2 4 6 8 *Depth of 10 mm 4TYP
Critical Design Features	Overhang with increasing surface area	Thin wall with changing cross-sectional profile	Overhang and thin wall geometry	Varying unsupported spans (gaps)
Rationale	Heat buildup due to steep overhang may lead to poor surface finish on the edges and microstructure coarsening	Narrow wall thickness and neck-area may cause heat build-up and poor surface finish	Poor surface finish on the underside of the overhang surface due to heat build-up	Overheating of gaps leading to distortion and loss of geometric integrity
Post Processing	X-ray CT, SEM, Microhardness, Surface Profilometry.	X-ray CT (Nominal-to-Actual comparison, Metrology), Optical microscopy		Visual Observation

number of parts on the build plate. In this work, no recoater impact was detected by the Hall effect sensor.

2.2. Build plan

2.2.1. Test parts

Two build plates with identical parts were created in this work, one termed *fixed processing* and the other termed *controlled processing*. The nominal settings for the build plate with fixed processing conditions are reported in Table 1. For fixed processing, nominal process parameter settings for Nickel Alloy 718 material were implemented based on recommendations from the powder manufacturer. These process parameters were optimized to avert porosity. Nickel Alloy 718 was chosen given its wide use in the aerospace and energy generation industries [53].

As shown in Fig. 5, each build plate consists of 16 parts encompassing 10 unique types of geometries. All the parts are 25 mm tall to prevent abrupt change in the time between layers resulting from early completion of certain parts, which can cause flaw formation [9,54]. Parts were placed near the center of the build plate to prevent flaw formation from lens aberrations, and a spacing of ~10 mm was maintained between parts to reduce the potential for inter-part thermal interaction. Total build time was approximately 15 h. Additionally, the build plate was preheated to 85 °C to mitigate residual stresses.

Four representative parts were selected for analysis in this work. Referring to Fig. 5, the parts selected are labeled: cone, vase, frame, and bridge. These four parts were selected for further analysis because their relatively compact size was conducive for post-process X-ray CT analysis and metallurgical characterization. The rationale for the design of these parts is described in Table 2, along with their respective post-processing steps.

After the fixed processing build plate was completed, the IR data from the cone-shaped part was used to calibrate the graph theory model. The model predictions are subsequently used to alter the processing conditions for the controlled processing build plate. The model calibration steps along with the approach for altering process parameters for the controlled processing build plate are explained in Sec. 2.4.

2.2.2. Time between layers (TBL) or Inter-layer time (ILT)

The X-Y area scanned by the laser varies substantially over the course of the build. The time between layers (TBL), also called inter-layer time (ILT), varies in proportion to the scanned surface area. The ILT is defined as the time elapsed between the beginning of melting one layer to the beginning of the succeeding layer.

The ILT is obtained from the slicing software before starting the build and verified with data from the recoater current sensor. Fig. 6 tracks the ILT as a function of build height and layers. The ILT varies from 80 ± 5 s for the first 5 mm (125 layers) to 70 ± 5 s thereafter. The ILT is a critical input, represented as τ [s], in the graph theory model, (Eqn. (4), Sec. 2.4). The ILT includes the 15 s constant time to recoat a fresh layer of powder.

In Fig. 6, the first sharp decrease in ILT occurs at 3 mm (layer 75). This decrease was caused by the completion of the large bases of several parts. Another decrease occurs at 10 mm (layer 250), where the surface area of several large parts was reduced. Beyond 20 mm build height (layer 500) the surface area of the cone increases in relation to the other parts, which proportionally increases the time to scan the layer. Therefore, the ILT gradually increases from layer 500 until the build was completed (Layer 625).

2.2.3. Post-process part characterization

After processing, the parts were examined ex-situ using a variety of non-destructive and destructive metallurgical characterization techniques. Non-destructive analysis included X-ray computed tomography (X-ray CT, Nikon XTH-225) for nominal-to-actual metrological analysis, and porosity measurements. The X-ray CT scanning resolution for these parts was 10 μm per voxel. The CT Pro 3D software was used to reconstruct the 3D volumes from the 2D projections acquired from the X-ray CT. The Volume Graphics software (VGSTUDIOMAX 3.3.4) was used for nominal-to-actual part comparison (NAC) and porosity analysis. The porosity content in each part is reported in terms of defect volume ratio (DVR).

In addition, the relative density of the parts was quantified using Archimedes measurements. Relative density is the ratio of the density of the sample compared to a fully dense sample of the same material. Samples with a relative density less than 100% are likely to be affected by porosity or other flaws [55]. The surface roughness of as-built parts was measured using laser scanning microscopy (Keyence VK-X200K). The surface roughness is quantified in terms of the average areal surface roughness (Sa), and is reported as the mean of 6 different sample regions, each of area 1 mm × 1.4 mm.

For microstructure characterization, the parts were cross-sectioned using wire electro-discharge machining. The cross-sectioned samples were ground using silicon carbide abrasive
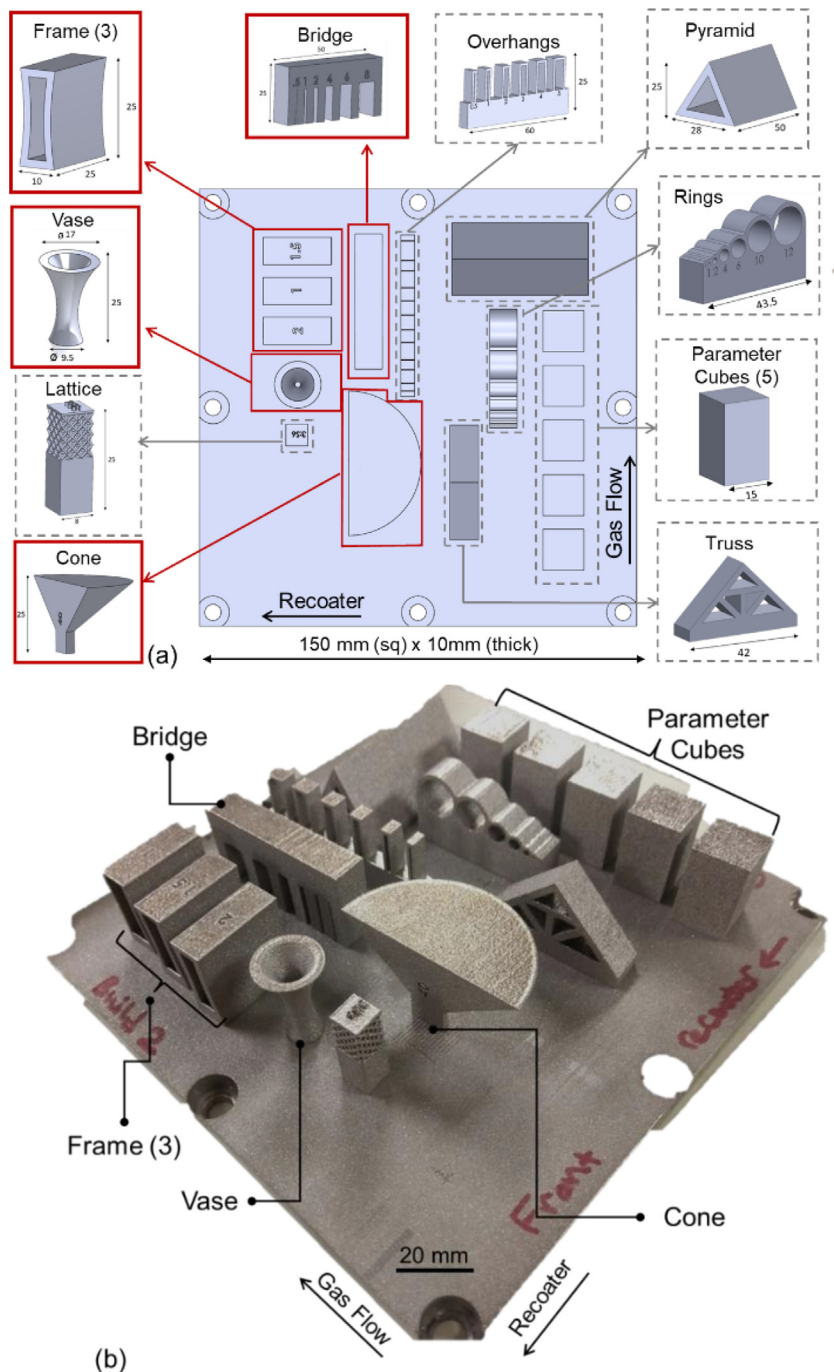
Fig. 5. (a) Top view of the build plate with detailed view of the 16 geometries created in this work. Four geometries (cone, vase, frame, and bridge) are analyzed in depth. (b) Actual fixed processing build plate upon completion.

paper, polished using diamond paste (3, 1, 0.5 µm) and etched with aqua regia for ∼10 seconds. Subsequently, optical and scanning electron microscopy (Helios 660 NanoLab, FEI) were used to analyze the microstructure. Microhardness measurements (Vickers, $H_{V0.5}$) were then acquired at 0.5 kg and dwell time of 10 s (Tukon 2500 Hardness Tester).

2.3. Temperature measurement

2.3.1. Calibration of IR thermal camera measurements

It is necessary to calibrate the thermal camera readings because IR thermography provides a relative measurement and not an absolute temperature reading [52,56,57]. The temperature measurements captured by the IR camera consider thermal emissivity to be constant. However, emissivity is not constant, but depends on the temperature of the body, angle of inclination of the body to the IR camera, and surface finish of the body [56]. In LPBF, the surface temperature varies considerably, and the surface texture transforms as the material changes from powder to a consolidated part. Accordingly, LPBF researchers have created rigorous calibration procedures to convert temperature readings obtained by the IR thermal camera to an absolute scale [57].

In this work, we conducted an offline two-point calibration after the parts were built to offset emissivity differences between un-
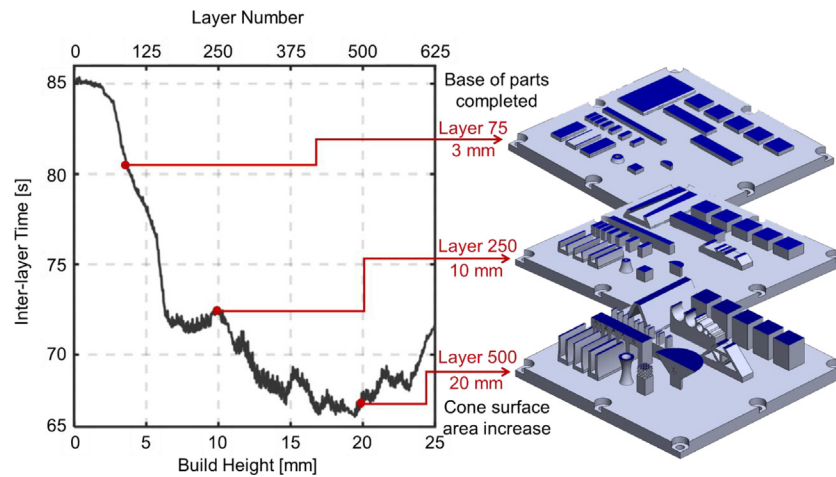
Fig. 6. The time between layers (TBL), or inter-layer time (ILT) changes significantly during the build. The ILT varies continually throughout the 625 layers (25 mm), from 85 s at the start of the build to 70 s at the end, reaching a minimum of ~65 s near 20 mm. The total build time was 15 h.

melted powder and solid metal parts. The temperature readings from the IR camera were converted to an absolute scale through direct correlation to temperature recorded by a contact thermocouple welded to two of the five cube-shaped parts which was selected for calibration (see Fig. 5). This industry-standard procedure, used in previous publications, is summarized as follows [8,23,58]. The following procedure is similar to the calibration methods recently reported by Wang *et al* [52].

After completing the first fixed processing build, two of the cube-shaped parts (Fig. 5) were removed from the build plate and a K-type thermocouple was resistance spot-welded to the surface of each part. The parts were placed on a fixture with a cartridge heater, which was bolted on the build plate of the machine. The calibration setup is shown in the inset of Fig. 7(b).

The build plate was lowered to place the top surfaces of the cubes at the level of the processing plane and the parts were placed in the same location as would be seen by the IR camera during the actual build, essentially recreating the process conditions inside the chamber during the build. Metal powder was deposited on top of the part to simulate the state of the process before laser melting. This is because the thermal emissivity values of an as-printed LPBF surface and a surface with powder spread on top dif-

fer significantly [9,26]. The temperature of the parts was gradually raised using the cartridge heater and the absolute temperature response of the thermocouple as well as the relative temperature response of the IR camera were recorded. The process was repeated without powder on top of the part to simulate the condition after a layer has been processed.

A calibration function was obtained by fitting a regression function to the recorded data for both the bare-metal and powder-deposited conditions. The result of the calibration and the fitted regression function are presented in Fig. 7(a) and Fig. 7(b) for the powder-deposited and bare-metal conditions, respectively. To reduce the effect of measurement noise, the IR reading was averaged over a 9 pixel × 9 pixel (180 μm × 180 μm) region, centered on each cube. The calibration functions shown in Fig. 7 range from 25 °C to 250 °C. Temperature measurements over the upper limit would be inaccurate as it would saturate the IR camera readings. These obtained calibration functions were applied to all IR measurements for this work.

We note that the calibration curves in Fig. 7 are valid for fixed intrinsic and extrinsic status of the IR camera. A change in the intrinsic state of the IR camera, i.e., the various software settings of the camera, such as exposure time, would void the calibration.
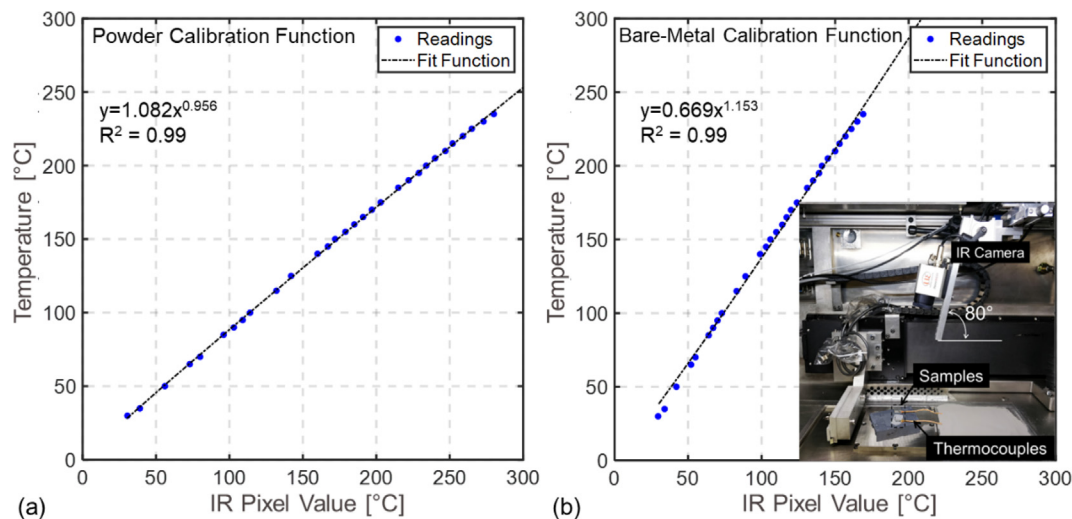
Fig. 7. Calibration functions for converting the IR thermal camera readings to absolute temperature measurements. (a) The calibration function for powder deposited on the part. (b) Calibration function for the bare-metal condition. Inset. The fixture used for calibration of the temperature readings.

Likewise, a change in the extrinsic state of the IR camera, i.e., angle of inclination, position, stand-off distance from the build plate, would also invalidate the calibration functions. Given the sensitivity of the sensor to both internal and external settings, using a part-level infrared thermal camera for closed-loop feedback control would further compound measurement errors.

In this work, measurement of the liquidus temperature was not attempted, as the focus is to predict and control the end-of-cycle temperature gradient after solidification, as opposed to local melting phenomena, and moreover, the temperature of the liquid state metal was beyond the saturation range of the camera sensor.

2.3.2. End-of-cycle surface temperature

An example of the IR thermal camera images acquired during the fixed processing build are shown at select intervals in Fig. 8. The temperature scale bar in Fig. 8 is obtained after applying the calibration function discussed in Sec. 2.3.1. These IR images, taken at the end of each layer, visually depict the variation in surface temperature observed in the various parts. For example, despite printing under identical processing conditions, Fig. 8 shows the prominent increase in surface temperature throughout deposition for the cone-shaped part compared to the other parts. Thus, the thermal history varies layer-to-layer for the same part, as well as between parts at the same layer. Hence, to avoid heat buildup, it is necessary to tailor the processing conditions both part-by-part and layer-by-layer.

The thermal history of the parts is quantified in terms of the end-of-cycle surface temperature. The end-of-cycle surface temperature, visually explained in Fig. 9, has been used in our previous works [99,22,24]. It is the average of the IR camera thermal readings after calibration over a 3 pixel × 3 pixel (60 μm × 60 μm) region on each part. The end-of-cycle surface temperature is plotted in Fig. 10 for each of the four parts studied in this work.

Fig. 9(a) shows an example of the selected 3 pixel × 3 pixel (60 μm × 60 μm) region of interest for the cone part. The surface temperature response for this region of interest over all 625 layers is shown in Fig. 9(b). We note that the temperature readings in Fig. 9(b) are obtained after converting the IR temperature readings to an absolute temperature scale using the two calibration functions described in Sec. 2.3.1.

On closer examination of the data from Fig. 9(b), periodic spikes are observed. In Fig. 9(c), spikes labeled (A) are caused by the laser scanning over the region of interest on the part. This is followed by a rapid cooling and slight increase after the powder bed is lowered and a new layer of powder is deposited. The rationale is explained in the schematic pictures on the last row of Fig. 9. The end-of-cycle temperature, demarcated at the temporal location (B) in Fig. 9(c), is recorded 0.5 s before the laser strikes a new layer of powder. The end-of-cycle temperature (B) is plotted as a function of the build layer for the cone-shaped part in Fig. 9(d).

The end-of-cycle temperature reported over the 60 μm × 60 μm region of interest for each of the four parts is shown in Fig. 10. This region of interest was chosen to enable measurement of thin cross-section regions in the vase and frame parts. Measurements near part edges were avoided to preclude errors due to image blurring between the part and surrounding powder. In Fig. 10, the temperature for the first 5 mm (125 layers) is not reported since the IR thermal camera readings are affected by transients from the cartridge heater used to preheat the build plate.

In Fig. 10(a), the end-of-cycle surface temperature for the cone-shaped part increases significantly due to the 45° overhang on the edge. In Fig. 10(b) for the vase part, the surface temperature increases after the narrow neck region due to the insulating nature of the powder trapped in the narrow internal cavity, the increase in overall surface area being consolidated, and the thin-wall nature of the part. Similar rapid increases in the end-of-cycle surface temperature for the frame part is evident in Fig. 10(c) at the overhanging section at the end of the build from ∼ 22 mm build height (layer 550) until completion. In the bridge-shaped part (Fig. 10 (d)), the surface temperature increases sharply after a build height of 15 mm (layer 375) as the relatively thin legs are poor pathways for conduction of heat trapped by unmelted powder in the gaps.

We note that the surface temperatures reported in Fig. 10 do not exceed 200 °C, which is well below the melting point of the material (Nickel Alloy 718, 1600 °C). This is because, as explained in the context of Fig. 9, the end-of-cycle surface temperature is obtained after a new layer of fresh powder has been deposited by the recoater, and 0.5 s before this new layer is melted. Since the inter-layer time (ILT) in this work (Fig. 6) was between 65 and 85 s, and given the rapid cooling rates observed in LPBF, the
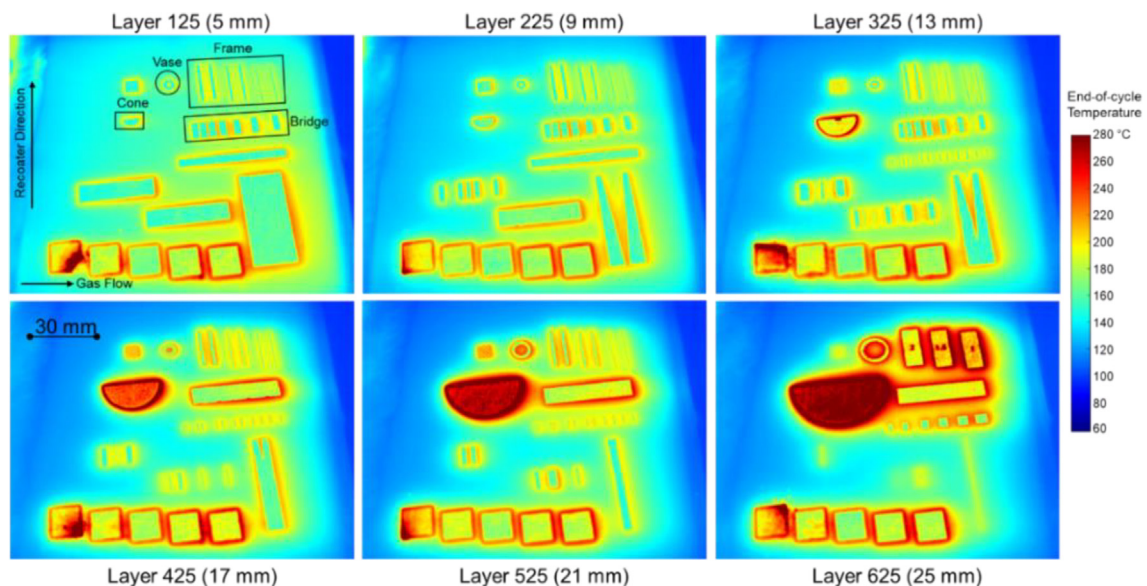
Fig. 8. Surface temperature images obtained from the IR camera during the fixed processing build. These images are taken after a layer is melted. Despite processing with constant processing conditions, the surface temperature during the build varies between parts at the same layer, as well as layer-to-layer for the same part. The scale bar is calibrated to absolute temperature.
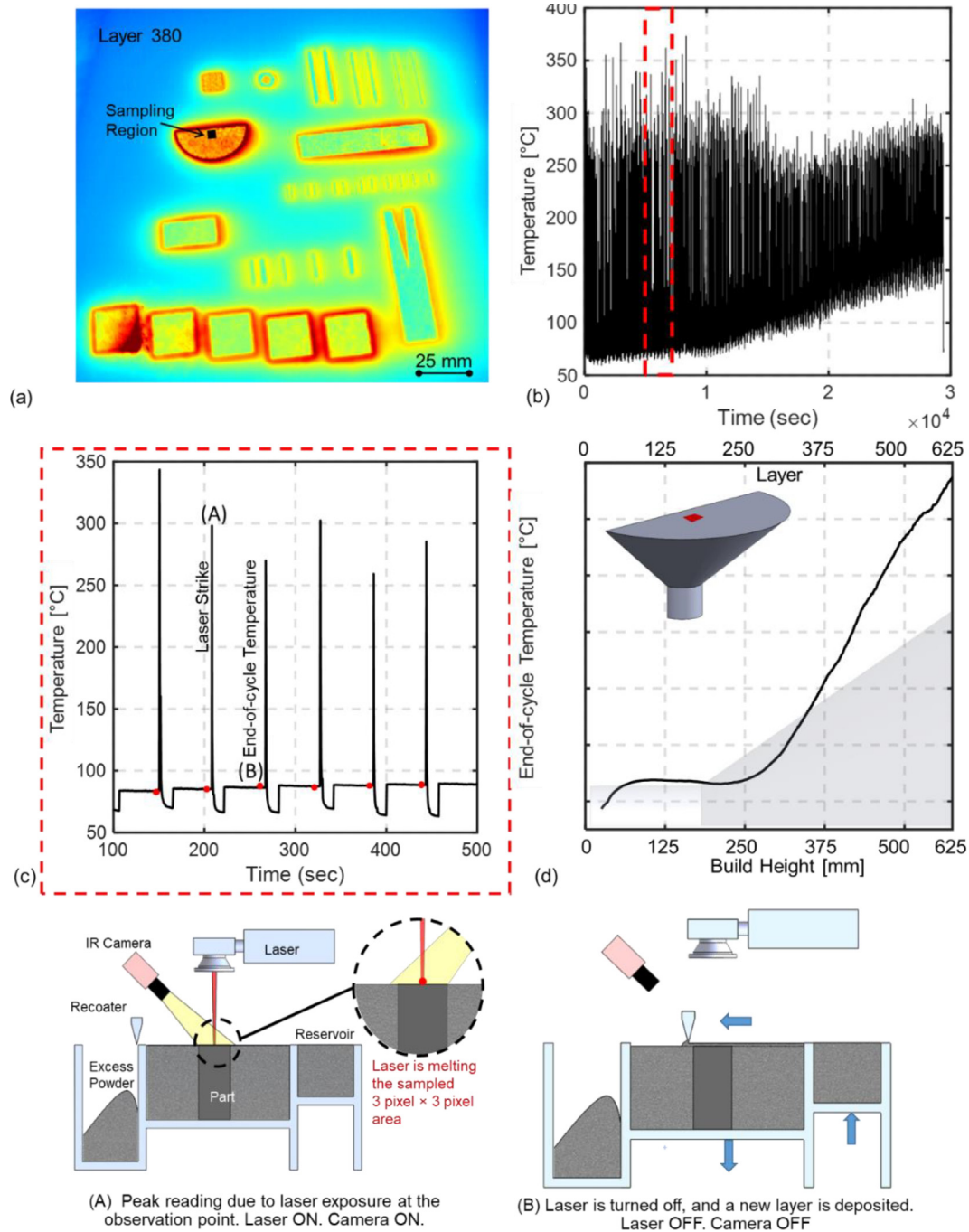
Fig. 9. Obtaining the end-of-cycle surface temperature from the IR camera. (a) a 60 × 60 μm (3 × 3 pixel) region of interest is selected for each part. (b) The temperature trends for each part are plotted. In this case, the trends for the cone are shown. (c) A zoomed-in view shows a prominent spike (A) caused due to laser events depicted in the two pictures. (d) The end-of-cycle temperature (B) is plotted across all layers. End-of-cycle temperature is extracted after a fresh layer of powder is deposited but 0.5 s before the next laser strike (A).

end-of-cycle surface temperatures are well under the melting point of the material.

2.4. Model-driven feedforward process control

2.4.1. Graph theory thermal modeling

2.4.1.1. Background – Solving the heat diffusion equation with graph theory. To predict the thermal history, it is necessary to solve the heat diffusion equation (Eqn (1)) [12,49,50,59]. In the heat diffusion equation, the temperature T at a point (*x,y,z*) at time (*t*) is,

$$\rho c_p \frac{\partial \mathrm{T}(x,y,z,t)}{\partial t} - k \overbrace{\left(\frac{\partial^2}{\partial x^2} + \frac{\partial^2}{\partial y^2} + \frac{\partial^2}{\partial z^2} \right)}^{Laplacian operator} \mathrm{T}(x,y,z,t)$$

$$= \frac{\mathrm{P}}{\mathrm{v} \cdot \mathrm{h} \cdot \mathrm{d} \cdot \mathrm{t}_0} \tag{1}$$
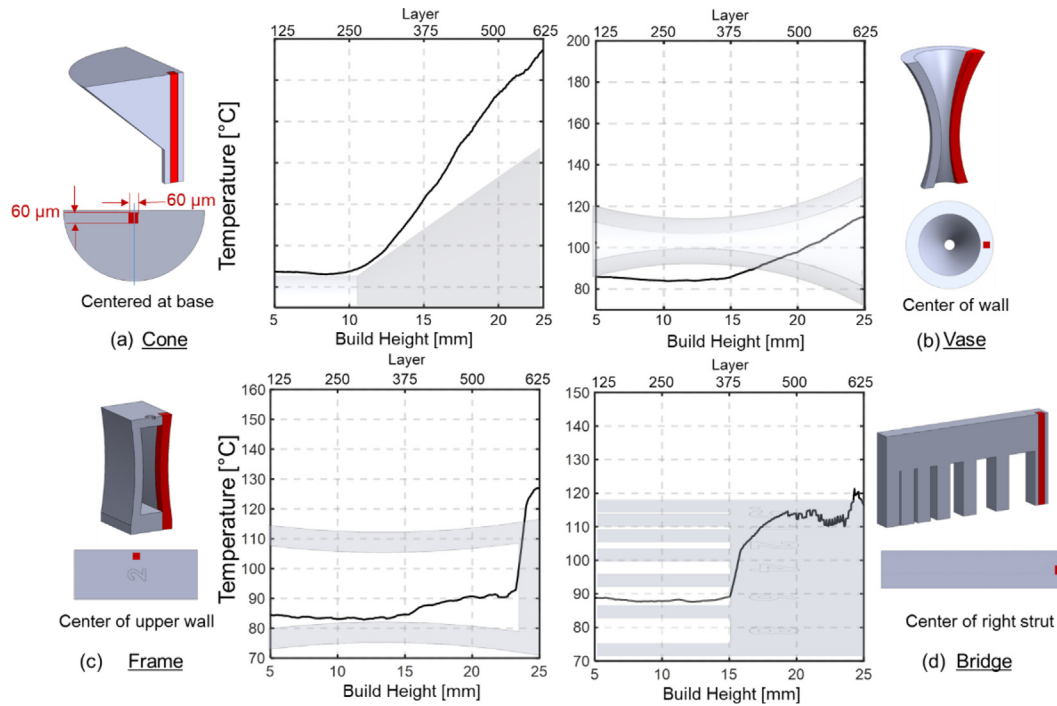
Fig. 10. Observed surface temperature from IR camera plotted as a function of layer height for: (a) cone, (b) vase, (c) frame, and (d) bridge. Also shown are corresponding locations where surface temperature are reported. A 60 μm × 60 μm region of interest corresponding to 3 pixel × 3 pixel in the IR camera image is selected for tracking the surface temperature across the layers.

The right-hand side of the heat diffusion equation captures the effect of processing parameters such as scan speed (v, [m·s⁻¹]), hatch spacing (h, [m]), laser power (P, [W]), layer height (d, [m]), and characteristic time (t₀, [s]). The characteristic time is the pulse time of the laser.

The right-hand side is further simplified as $E_V = \frac{P}{v \times h \times t \times t_0}$ [W·mm⁻³], which is called the volumetric energy density and is defined as magnitude of energy supplied by the laser to melt a unit volume of powder [55,60,61]. This form of the heat diffusion equation is commonly used for thermal modeling in LPBF [50].

The left-hand side of the heat diffusion equation includes material properties: density (ρ [kg·m⁻³]), specific heat (c_p [J·kg⁻¹·°K⁻¹]) and thermal conductivity (k [J·m⁻¹·s⁻¹·°K⁻¹]). The second derivative term in the heat equation, $\frac{\partial^2}{\partial x^2} + \frac{\partial^2}{\partial y^2} + \frac{\partial^2}{\partial z^2}$, called continuous Laplacian operator, is expressed in terms of spatial coordinates of the body, and thus captures the effect of part shape on the heat flow.

The heat diffusion equation is solved by adding the following boundary and initial conditions, and by replacing the heat source term E_V with an initial temperature distribution $T_0(x, y, z)$. In Eqn. (2), below, the continuous Laplacian operator is represented as ∇^2 and the thermal diffusivity as $\alpha = \frac{k}{\rho c_p}$ [m² ·s⁻¹].

$$\frac{\partial T(x,y,z,t)}{\partial t} - \alpha \nabla^2 T(x,y,z,t) = 0 \quad \text{(For one heating cycle)}.$$

$$T(x,y,z,t=0) = T_0(x,y,z) \tag{2}$$

$$\frac{\partial T(x,y,z,t)}{\partial n} = 0 \quad \text{(On boundary)}$$

Shifting the heat source to the initial condition is reasonable for the LPBF where the laser scan is rapid compared to the long dwell time before the next layer is melted. The initial temperature distribution $T_0(x, y, z)$ contains the melting temperature of the material, and the initial temperature in the remainder of the body is the

temperature distribution from the previous heating cycle. Initial node temperatures are assumed to be the preheat temperature of the build plate (85 °C).

Lastly, the boundary condition implies no heat is lost to the surroundings from the boundaries of the body; $\frac{\partial T(x,y,z,t)}{\partial n}$ is the outward normal vector. Heat loss at the boundaries is addressed in a separate step (Step 3) during practical implementation as discussed later in Sec 2.4.2. We note that the forgoing simplification is common to thermal modeling in LPBF [50].

The graph theory approach approximates the continuous Laplacian with the graph Laplacian matrix L, in effect, $\nabla^2 = -L$ as discussed in depth in our previous work [28]. The solution is obtained by discretizing the heat diffusion equation over N nodes and by replacing the continuous temperature with a discrete temperature vector (T),

$$\frac{\partial T(x,y,z,t)}{\partial t} + \alpha L T(x,y,z,t) = 0 \tag{3}$$

The above first-order ordinary linear differential equation has the following solution,

$$T(x,y,z,\tau) = \phi e^{-\alpha g \Lambda \tau} \phi' T_0(x,y,z) \tag{4}$$

Eq. (4) frames the heat diffusion equation in terms of eigenvalues Λ and eigenvectors ϕ of the graph Laplacian L; T_0 [K] is the input temperature of the model, which is determined by the laser heating and temperature of previously deposited layers; τ [s] is the inter-layer time (ILT, Fig. 6); and g is a tunable *gain* factor [unitless], which controls the rate of heat diffusion and is discussed in depth by Cole *et al.* in[28].

The graph theory solution in Eqn. (4) is semi-analytic in nature, it is analytic in time and numeric in space. To avoid truncation errors, the entire eigen spectrum consisting of N (number of nodes) eigenvectors (ϕ) and eigenvalues (Λ) are considered. The input temperature (T_0 (x,y,z)) is estimated as a function of the laser power (P) as follows.

$$T_0(x, y, z) = T_{nom} \times \frac{P_{new}}{P_0} \beta \qquad (5)$$

where T_{nom} = 1600 °C is the melting temperature of nickel alloy 718 at the nominal laser power of P_0 = 285 W; P_{new} is the altered laser power, and β = 0.95 is a constant. The value of β was obtained through tuning of the graph theory model; it remains constant for all parts on both the fixed and controlled build plates. The value for P_{new} is bounded between 200 W and 370 W. The rationale, as described in Sec. 2.4.4, is to avoid lack-of-fusion porosity on the lower end and keyhole melting on the higher end of the laser power.

The variable for time τ in Eq. (4) serves as the effective time for cooling between laser strikes over the course of the build. Time is bounded from the time of laser strike τ = 0 to the interlayer time for the experiment (Fig. 6, Sec. 2.2.2) for a single layer. The gain factor (g) is added to calibrate the model for the specific machine and material. The value of g = 1.7 is functionally identical to our previous works, and its significance is discussed in detail in Yavari *et. al.* [23,26].

The graph theory approach to thermal modeling has the following advantages compared to traditional finite element analysis (FEA) based techniques in the context of LPBF [27].

(1) *Mesh-free Modeling.* The graph theory technique discretizes the part geometry into point nodes and does not need to mesh the part into volumetric elements. Whereas FEA requires repeated meshing and remeshing to simulate layer-by-layer deposition of LPBF, the graph theory model activates discrete nodes, saving computation time.

(2) *Matrix inversion-free computation.* Unlike FEA, the graph theory solution does not involve cumbersome matrix inversion steps. Instead, the eigenvalues (Λ) and eigenvectors (ϕ) of the Laplacian matrix (L) are used, which further reduces computation time.

(3) *Time-step free calculation.* The FE approach is a fully numeric computational solution which requires time steps to be small for the solution to converge. The graph theory solution is analytic in time, hence the time step (τ) in the graph theory solution, shown in Eqn. (4) can be set to any value without losing precision [27,28]. Thus, the graph theory simulation does not require stepping through time.

2.4.1.2. Prior work in graph theory thermal modeling. Our prior publications have compared the computational accuracy and efficiency of the graph theory approach in relation to exact Green's function-based analytical solutions, finite element, and finite difference methods for benchmark 1D and 3D heat transfer problems [24,28]. These prior works also delineate the effect of number of nodes and influence of boundary conditions. From a computational perspective, the approach typically converges to within 1% of the exact analytical solution approximately 2.5 to 5 times faster than finite element models.

Prior work has also involved practical application of the graph theory approach to thermal modeling of the LPBF process, including: (1) verification of the graph theory model predictions with proprietary (Netfabb) and non-proprietary FE software [27]; (2) validation of model predictions with experimental temperature observations for several part shapes, including large complex LPBF parts [23,26]; and (3) correlation of thermal history predictions with porosity, microstructure evolved, and thermal-induced failures [9,25]. Recently, the graph theory approach was extended to thermal modeling of the directed energy deposition process [62]. These prior works affirm that the graph theory solution converges

in ~1/10th of the time of non-proprietary FE models, with error less-than 3%.

2.4.2. Thermal modeling of LPBF parts using graph theory

Fig. 11 shows the four steps in the application of the graph theory approach to model the thermal history of LPBF parts. In Step 1, the part geometry is discretized into point nodes. These nodes are sampled with a uniform random distribution throughout the part geometry.

The node density (n, nodes·mm^{-3}) impacts the convergence of the model as shown in previous work [26-28]. A higher node density (n) results in a more accurate convergence, albeit at the expense of computation time. The computation scales exponentially (n^3) to the number of nodes [23,27,28].

In Step 2, the nodes are connected by edges, whose weight depends on the Euclidean distance to neighboring nodes. From this connectivity information, the Laplacian matrix (L) is obtained, wherefrom the eigenvectors (ϕ) and eigenvalues (Λ) are computed. In step 3, the deposition process is simulated for each layer. Step 3 involves solving the heat conduction equation in Eqn. (1) for a layer using the graph theory approach (Eqn. (4)).

After heat diffusion via conducted, heat loss at nodes on the boundary of the part due to convection and radiation from the part to the surrounding powder, and from the part to the substrate is accounted by applying lumped capacitive theory to the temperature, as follows [9].

$$T_b = e^{-h\Delta t}(T_{bi} - T_p) + T_p \qquad (6)$$

Here, the temperature of the surroundings T_p is considered as constant, T_{bi} is the boundary node temperature obtained by the heat diffusion alone in Eq. (4), T_b is the resulting boundary node temperature incorporating convection and radiation heat loss, Δt is the time step between the calculation of the heat diffusion within a layer, and h [W·m^{-2}·°C^{-1}] is the bulk coefficient of heat loss for convection (via Newton's law of cooling) and radiation (via Stefan-Boltzmann law) from the boundary nodes to the surrounding powder and air. The heat loss coefficient is stratified between part to surrounding powder (h_w), and part to substrate (h_s). In addition to convection and radiation, heat loss via conduction between the part and the substrate is also included in h_s. After convection and radiation are adjusted at boundary nodes, the temperature at various nodes obtained from graph theory at each node located at position (x, y, z) at time step Δt is $T(x, y, z, \Delta t)$.

Lastly, in Step 4, Steps 1 – 3 are repeated as required to simulate the layer-by-layer process. At the end of each iteration, the temperature of the previous layers is carried forward. Hence, residual heat from deposition of previous layers is retained in the nodes. The simulation parameters used in this work are reported in Table 3. At the end of Step 4, the thermal history of all node locations is obtained and recorded. The result is a 3D rendering of the thermal history. The graph theory thermal model used here makes the following simplifying assumptions:

(1) Several layers are deposited at once to reduce computation time. This so-called super layer or meta layer assumption is commonly used in both research and commercial FE-based thermal simulation implementations [49,51].

(2) The entire super layer is assumed to be deposited at the input (melting) temperature T_0. The shape and temperature distribution of the laser beam is ignored, and the laser is considered as a point source.

(3) Each part is considered independent from the others on the build plate, and parts are considered insulated from one another; the temperature of one part does not affect others.
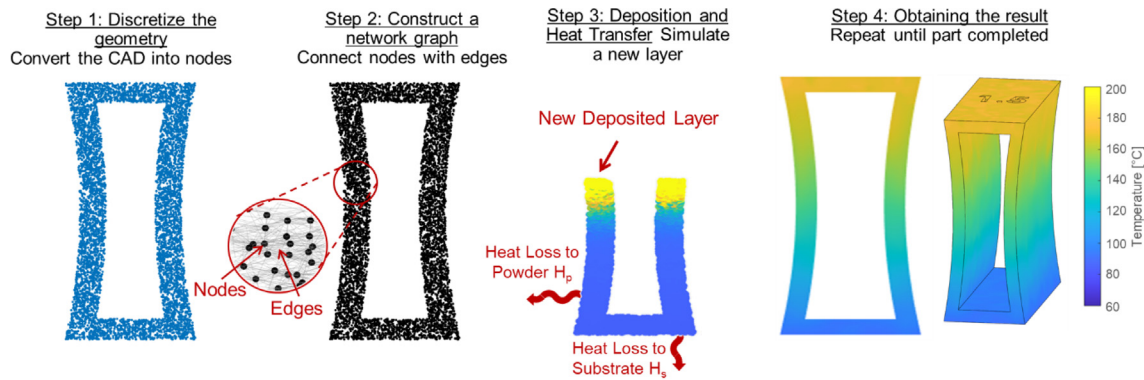
Fig. 11. Application of graph theory thermal modeling in LPBF showing four steps in simulating the thermal history of the frame part. A 2D map is shown here for explanation purposes, a 3D temperature distribution is obtained in practice for each layer.

Table 3
Simulation parameters used in the graph theory thermal simulation [9].

Simulation Parameters	Values
Heat loss coefficient part to powder, h_w [W·m^{-2}· °C]	2.8
Heat loss coefficient part to substrate, h_s [W·m^{-2}· °C]	80
Thermal Conductivity (k) [W·m^{-1}·°C]	19.47
Density (ρ) [kg·m^{-3}]	8,193
Specific Heat (c_p) [J·Kg^{-1}·°C^{-1}]	435
Melting Point (T_0) [°C]	1,600
Ambient chamber temperature, T_p [°C]	85
Characteristic length [mm]	2
Neighborhood distance (ε) [mm]	5
Maximum number of nearest neighbors (n)	6
Superlayer thickness [mm]	0.5 (12.5 actual layers)
Gain factor (g) [unitless]	1.7
Computational hardware	AMD Ryzen 3970X CPU, @3.70 GHz with 128 GB RAM.

(4) Heat loss through conduction, convection both free and forced, and radiation are considered, however, the effect of latent heat of fusion due to transformation of material from solid to liquid and back to solid is ignored. Therefore, meltpool-scale phenomena are ignored.

2.4.3. Model calibration

To utilize the graph theory thermal modeling approach (Eqn. (4)), three modeling parameters must be calibrated, these are the gain factor (g), the number of nodes (n), and super-layer thickness (s). The super layer or meta layer assumption, where several layers are assumed to be deposited at once, is used commonly in thermal simulations of LPBF to speed computation [12]. The data obtained for the cone-shaped part was chosen for model calibration. Based on previous work for the same material, the gain factor was fixed as g = 1.7 [unitless] [9].

The graph theory solution was obtained for various values of node density (n) and super layer thickness (s) and compared with the IR data. The error with respect to the IR data is reported in Table 4 in terms of the mean absolute percentage error (MAPE, %), and root mean squared error (RMSE, °C). The values of n and s resulting in the least MAPE, and RMSE are selected. The effect of node density (n) with s = 0.5 mm on convergence is shown in Fig. 12(a) and Table 4(a). Likewise, the effect of layer thickness (s) with node density n = 0.5 nodes·mm^{-3} is shown in Fig. 12(b) and Table 4(b).

Referring to Fig. 12(a) and Table 4(a), increasing the node density (n) results in accurate convergence at the cost of computation time. Similarly, from Fig. 12(b) and Table 4(b), reducing the super layer thickness (s) improves the model accuracy, but involves a tradeoff in computation speed. Based on extensive offline tuning, in this work we select n = 0.5 nodes·mm^{-3} and s = 0.5 mm (Table 3). With these settings, the MAPE and RMSE with respect to the end-of-cycle surface temperature measurements for the cone-shaped part are 1.16% and 4.5 °C, respectively, and the simulated thermal history was computed in under five minutes on the desktop computer specified in Table 3.

2.4.4. Implementation of feedforward process control

(a) Control design

This work implements a heuristic feedforward control approach. The approach has three steps, namely, (Step 1) predict; (Step 2) analyze; and (Step 3) correct. The approach is summarized in Fig. 13 in the context of the cone-shaped part.

First, in Step 1, the thermal history of the part is predicted using nominal processing conditions. As depicted in Fig. 13(a), it is observed that the end-of-cycle surface temperature increases rapidly after 12 mm of build height (layer 350). In this work, an increase in end-of-cycle surface temperature greater than 20 °C between successive super layers was considered as a potential onset of heat buildup [9]. This threshold was selected based on previous work with the same material and LPBF system. Based on this criteria, in Step 2 (analyze, Fig. 13(b)), the surface temperature after 12 mm (300 layers) is flagged as a point of heat buildup.

In Step 3, the steep rise in end-of-cycle surface temperature was remedied by reducing the laser power and increasing the dwell time between layers. For this purpose, the thermal history was simulated iteratively using the reduced laser power as an input for the graph theory model (Sec. 2.4.1). An increase in dwell time is considered and tested in the simulation, only if decreasing the laser power to 185 W does not mitigate heat buildup.

(b) Parameter bounds

For this work, it was determined that the laser power should be maintained within ± 30% of the nominal laser power (P_0 = 285 W) to ensure suitable levels of consolidation and density; these limits translate to 200 W (-30% P_0) and 380 W (+30% P_0). These bounds were based on the porosity and relative density analysis results from five cube-shaped parts (10 × 10 × 25 mm) shown in Fig. 5.

Each of the cubes were printed with varying laser power levels while the rest of the processing parameters were identical to the parameters listed in Table 1. The laser power levels tested were,

Table 4
(a) Convergence results for the graph theory model as a function of node density (n), the super layer height was fixed at s = 0.5 mm. (b) Convergence results for the graph theory model as a function of super layer thickness with node density was fixed at n = 0.5 node·mm^{-3}. The number in parenthesis is the std. dev over 10 iterations.

Node Density (n) (node·mm^{-3})	n = 0.2	n = 0.3	n = 0.4	**n = 0.5 (selected)**
MAPE (%)	5.42 (1.05)	4.73 (1.24)	3.44 (0.95)	**1.16 (1.01)**
RMSE [°C]	24.0 (4.6)	19.7 (5.4)	13.2 (3.8)	**4.5 (3.5)**
Average Run Time [s]	83	140	221	**305**
Layer Size (s (mm)	**s = 0.5 (selected)**	s = 0.6	s = 0.8	s = 1.0
MAPE (%)	**1.16 (1.01)**	2.46 (2.93)	5.50 (2.93)	5.67 (3.05)
RMSE [°C]	**4.5 (3.5)**	14.5 (15.3)	62.7 (16.3)	39.2 (19.9)
Average Run Time [s]	**305**	208	184	141
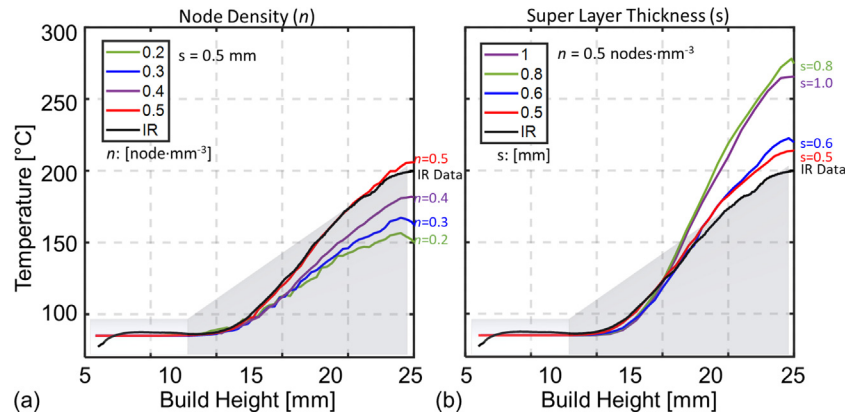
Fig. 12. Calibration of graph theory parameters, node density (n) and super layer thickness (s) using the cone part as reference. The IR measurements are used as ground truth, and plotted in in black. (a) The effect of changing node density (n) with super layer thickness fixed at s = 0.5 mm. (b) Effect of super layer thickness (s) with number of node n = 0.5 nodes·mm^{-3}.
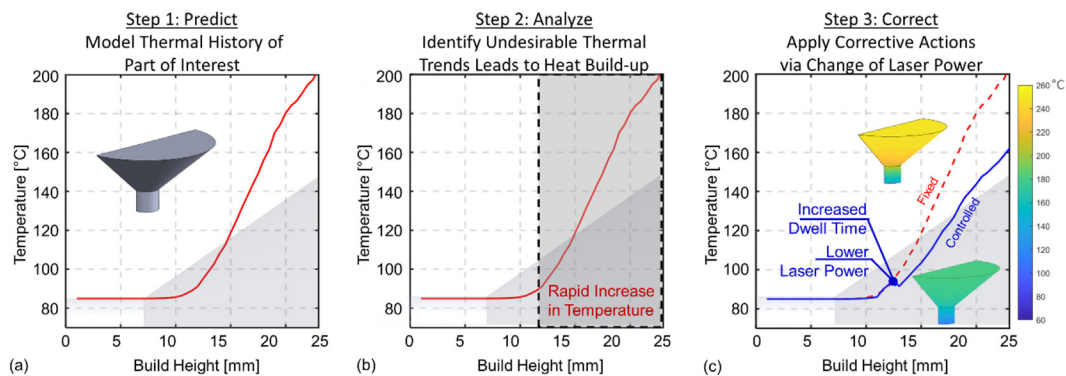
Fig. 13. The model-driven feedforward control of additive manufacturing approach applied to the cone-shaped part. (Step 1) Prediction - The graph theory thermal model is used to predict the thermal history of the part. (Step 2) – Instances of rapid increases in temperature (heat buildup) are identified from analysis of the thermal history predictions. (Step 3) – Thermal history is corrected to avoid steep temperature gradients and heat buildup by changing the laser power.

385 W (+35% P_0), 342 W (+20% P_0), 285 W (P_0), 228 W (-20% P_0), 185 W (-35% P_0). The parts were examined using X-ray CT and validated using the Archimedes method of density measurement. The porosity in the samples, in terms of the defect volume ratio (DVR), and the results of the Archimedes relative density measurements (ρ_{rel}), are presented in Fig. 14.

Lack-of-fusion porosity was observed when the laser power was set to 228 W (-20% P_0), resulting in a 0.87% DVR and ρ_{rel} = 95.3%; the lack-of-fusion porosity becomes severe at 185 W (-35% P_0) with a DVR of 1.37% and ρ_{rel} = 93.6%. Consequently, to avoid severe lack-of-fusion porosity during the model-driven feed forward control approach, the lower limit for laser power was found to be −30% P_0 = 200 W. To reduce overheating and keyhole mode operation, the upper limit for laser power was found to be + 30% P_0 = 370 W [63].

As evidence of the suitability of these laser power bounds and other constant processing parameters, none of the parts studied in this work, either produced under fixed or controlled processing conditions, showed evidence of lack-of-fusion porosity when examined with non-destructive X-ray CT and destructive metallography.

(c) Application

Having established the upper and lower limits of laser power for Nickel Alloy 718 in the context of porosity, each part was simulated iteratively as a function of laser power and dwell time. The
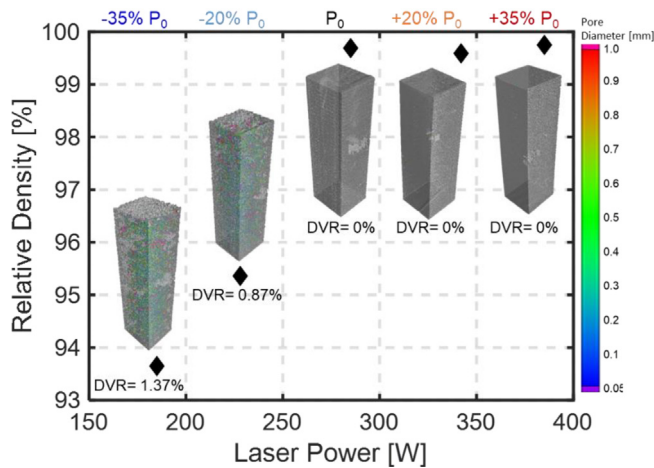
Fig. 14. Porosity levels (DVR) from X-ray CT and relative density (ρ_{rel}) from Archimedes measurements are plotted as a function of laser power (P) used for five the parameter cubes (Fig. 5). The nominal laser power, $P_0 = 285$ W. Severe lack-of-fusion porosity is observed when reducing laser power to 185 W (-35% P_0). Hence in this work, the minimum allowable laser power reduction for controlled processing was set to 200 W (-30% P_0). The maximum allowable power was set to 380 W (+30% P_0) to avoid overheating and keyhole melting. None of the four parts studied in this work, created either in fixed or controlled conditions, showed presence of porosity.

control target is the rate of change of end-of-cycle temperature, and is set at 0 °C/layer. The control is initiated when the rate of change (slope) exceeds 20 °C/layer. For ease of practical implementation, the dwell time and laser power were changed only once for each of the four parts, since these parameter changes are manually implemented by altering the G-code. The laser power and dwell time alterations for controlled processing of each of the four parts is unique and summarized in Fig. 15.

As an example, referring to Fig. 13(c), in the graph theory simulations the laser power for the cone-shaped part was reduced to 200 W from 285 W beginning at layer 300 (build height 12 mm). The reduced laser power was maintained until the end of layer 625 (25 mm). However, it was predicted that the steep increase in temperature of the cone-shaped part would not overcome despite reducing the laser power to 200 W (-30% P_0).

Decreasing the laser power below 200 W would risk severe lack-of-fusion porosity. Consequently, a 10 s dwell time was added to the inter-layer time (ILT) after the first 12 mm (300 layers) of build height. Likewise, for the vase and bridge-shaped parts, the power is reduced to 228 W from layer 375 onwards (15 mm). Similarly, the laser power for the frame was reduced to 228 W from layer 500 (20 mm) onwards.

While addition of a dwell time between layers can mitigate heat buildup, it also affects the thermal history of all the parts on the build plate. Moreover, increasing dwell time increases the produc-

tion time. For example, adding a 10 s dwell time after each layer from layer 300 onwards until layer 625 increased the build time by 1 h to approximately 16 h. Hence, from a productivity perspective the addition of the dwell time must be utilized sparingly. The thermal history, as a result of reduced laser power (200 W) and increased dwell time, is shown in Fig. 13(c).

3. Results and discussion

### 3.1. Cone

3.1.1. Thermal history

In Fig. 16(a) and (b), respectively, the model-derived end-of-cycle surface temperature trends are compared to the IR-measured end-of-cycle surface temperature measurements for the cone-shaped part produced under fixed and controlled processing. The significant increase in the end-of-cycle top surface temperature for the fixed-processed cone beyond layer 300 (12 mm), evident in Fig. 16(a), is accurately predicted by the graph theory model (MAPE 1.6%, RMSE 7 °C). Moreover, the simulation required approximately 4 min (234 s) of computation time.

The controlled processing of the cone involved reducing the laser power at layer 300 (12 mm build height) to 200 W from 285 W. Further, the recoater dwell time is increased by 10 s from layer 300 onwards. In Fig. 16(b), these two aspects substantially arrested the end-of-cycle surface temperature increase for controlled processing. Consequently, the end-of-cycle surface temperature is restricted to a maximum of 150 °C (Fig. 16(b)) for the controlled processing condition, compared to 200 °C for fixed processing (Fig. 16(a)).

The simulated spatial temperature distribution for the fixed and controlled processing of the cone-shaped parts at select layers is graphically compared in Fig. 17. In accordance with the temporal thermal history trends discussed in the context of Fig. 16, controlled processing significantly reduced the heat buildup in the bulk part. Further, the spatial temperature gradient of the controlled-processed part is relatively smaller compared to its fixed-processed counterpart.

3.1.2. Part quality – surface roughness, microstructure evolution, and microhardness

The reduction in surface temperature, as well as the spatial temperature gradient achieved on account of controlled processing (Fig. 16 (b)) has a significant impact on: part surface finish, microstructure grain size, and microhardness. For example, shown in Fig. 18 is an X-ray CT slice of the two cones, along with an optical microscope image of the slanted overhang edges. Both samples had no detectable levels of porosity using X-ray CT, resulting in a DVR of 0.00%. In the case of the fixed-processed cone, Fig. 18(a), the excessive heat buildup caused partially melted satellite powder
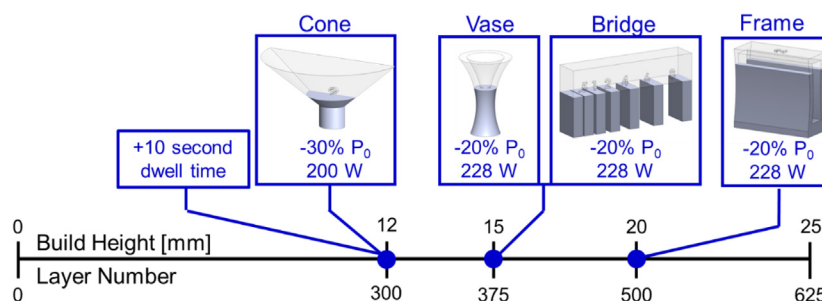

Fig. 15. Summary of process parameters adjusted for controlled processing of the four parts. Once the laser power is reduced at a layer it is maintained until the end of processing.
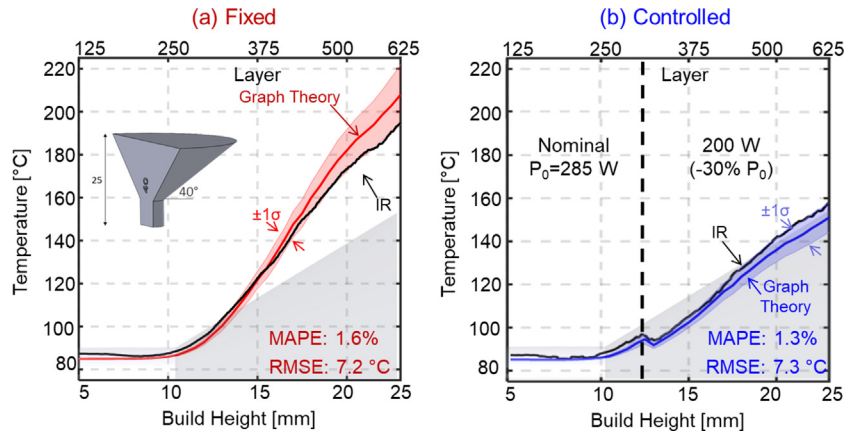
Fig. 16. (a) Predicted surface temperature trends overlaid on IR derived observation of the cone for. (a) fixed processing, (b) controlled processing. Note the steep increase in temperature in (a) compared to (b) after ∼ 12 mm build height (layer 300). These simulations required less than 4 min of computation time with error less than 2% (MAPE). The graph theory simulation is repeated 10 times and the ± 1σ prediction bands are plotted. The gray area in the background represents the shape of the part in terms of the build height.
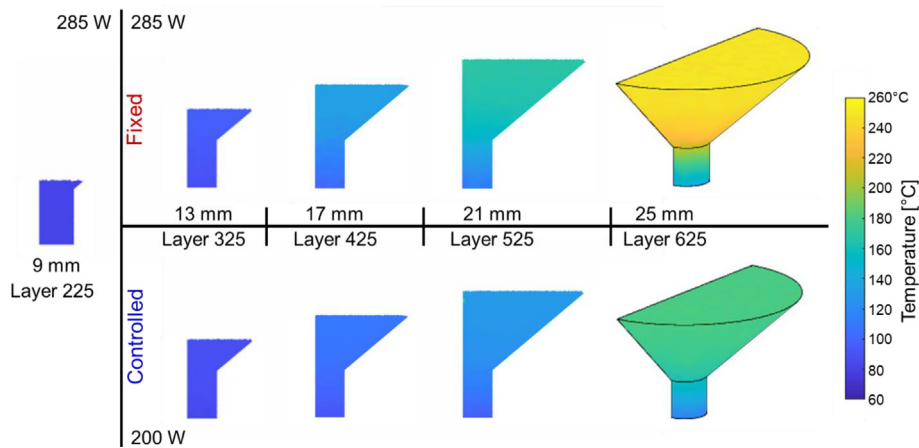
Fig. 17. Spatial temperature distribution for the cone part predicted using the graph theory thermal model for fixed processing (top) and controlled processing (bottom). In controlled processing heat buildup and spatial temperature gradients are significantly reduced by decreasing the laser power to 200 W from layer 300 onwards.
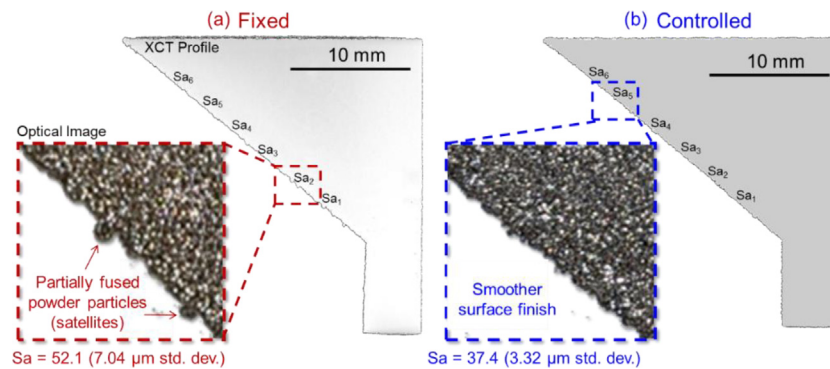
Fig. 18. X-ray CT and optical images of the cone-shaped parts. (a) Fixed processing resulted in a rougher surface finish (Sa ≈ 52 μm) due to partially fused particles (satellites) attached to the overhang edge. (b) Controlled-processed cone has a smoother surface finish (Sa ≈ 37 μm) without satellite particles.

particles to adhere to the overhang edge. However, the occurrence of satellite powder particles is mitigated for the controlled-processed cone (Fig. 18(b)).

As a result of partially melted powder adhered to the surface, the average areal surface roughness (Sa) at the overhang edge for the fixed-processed cone was assessed to be Sa ≈ 52 μm compared to Sa ≈ 34 μm for the controlled-processed cone. The foregoing

areal surface roughness measurements are averaged over 6 sample regions spaced along the overhang section (demarcated with Sa in Fig. 18), each region having an area of 1 mm × 1.4 mm. We also note that no lack-of-fusion porosity was observed in Fig. 18 for either the fixed-processed or controlled-processed cone.

The effect of temperature distribution on the microstructure of the fixed and controlled processing cone-shaped parts is presented

in Fig. 19. It was anticipated that heat buildup and an increased spatial temperature gradient in the fixed-processed cone-shaped part would result in larger grain size compared to the controlled processing parts. After cross-sectioning the parts with electro-discharge machining and polishing and etching the surface as described in Sec. 2.2.3, the microstructure was examined at different locations using scanning electron microscopy (SEM).

To quantify the grain size, the primary dendritic arm spacing (λ_1) was measured. The primary dendritic arm spacing (λ_1) is inversely proportional to the cooling rate, and hence provides an indirect means to verify the effectiveness of the controlled processing [9,64]. These measurements were made over a length of 20 μm, perpendicular to the dendrite growth direction. Four of the locations where the primary dendritic arm spacing (λ_1) was measured

is visualized in Fig. 19. These locations are demarcated as A, B, C, and D.

Until the 300-layer mark (12 mm), both the controlled and fixed-processed samples were measured to have $\lambda_1 \sim 0.68$ μm. However, after the laser power is changed from 285 W to 200 W at layer 300 (12 mm), λ_1 at locations for the controlled samples were consistently smaller than their fixed-processed counterparts. The λ_1 for the controlled-processed samples (200 W) was measured to be 0.49 μm ± 0.02 μm (Fig. 19(b)). By contrast, for fixed processing (285 W), Fig. 19(a), λ_1 = 0.69 μm ± 0.02 μm. Indeed, enlarged images of the overhang locations in Fig. 19(a) show the presence of secondary dendrites in the fixed-processed samples, symptomatic of excessive heat buildup [65].

Continuing with the analysis, λ_1 measured for the four locations A, B, C, D are plotted in Fig. 20(a). The λ_1 measurements are signif-
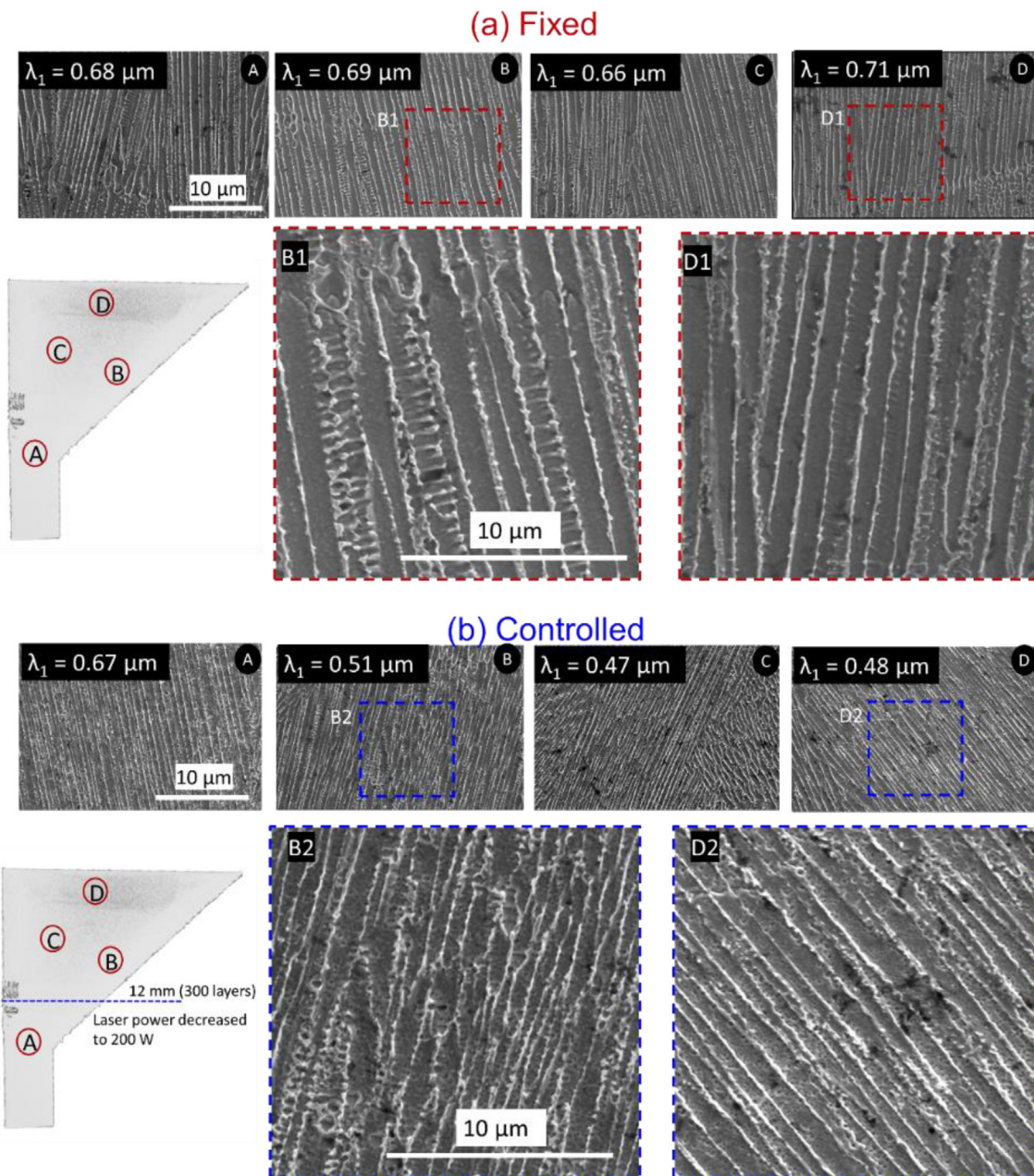
Fig. 19. Primary dendritic arm spacing (λ_1) measured along the build height for the (a) fixed, and (b) controlled processing cone-shaped parts at four locations (A), (B), (C), and (D). The mean primary dendritic arm spacing (λ_1) for the fixed processing part was $\lambda_1 \sim 0.65$ μm compared to $\lambda_1 \sim 0.50$ μm for controlled processing after the laser power was reduced to 200 W at layer 300 (12 mm) and a dwell time was increased by 10 s.
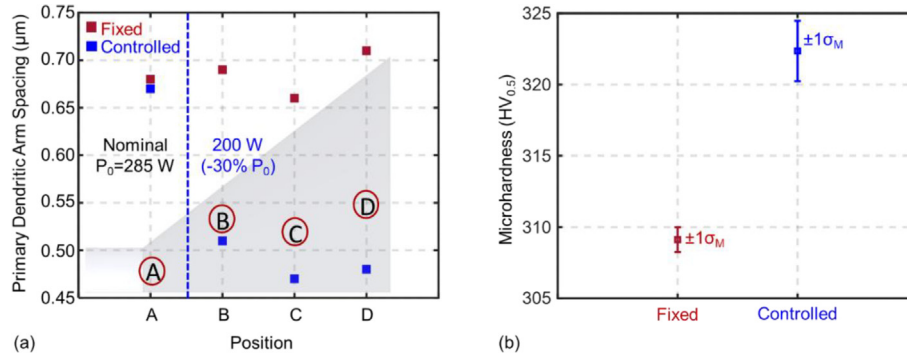
Fig. 20. (a) Primary dendritic arm spacing (λ_1) for controlled processing (blue) and fixed processing (red) conditions at the four positions A-D demarcated in Fig. 19. Reduction in laser power for sections B-D during controlled processing results in finer grain structure (smaller λ_1). (b) The microhardness ($HV_{0.5}$) is inversely related to λ_1 - the larger the grain size, smaller the microhardness. (For interpretation of the references to colour in this figure legend, the reader is referred to the web version of this article.)

icantly different for the fixed and controlled-processed samples at locations B, C, and D. This difference in λ_1, in turn, translates to a large difference in microhardness. As evident in Fig. 20(b) the smaller grain size of the controlled-processed samples results in a significantly higher average microhardness (HV_{05} greater than 320) compared to the fixed-processed cone part ($HV_{05} \sim 290$).

3.2. Vase

3.2.1. Thermal history

The predicted and IR-observed surface temperature trends for the vase part built under fixed and controlled processing are shown in Fig. 21(a) and (b), respectively. As evident from Fig. 21 (a), a steep increase in the end-of-cycle surface temperature of the fixed-processed cone was predicted after 15 mm build height (layer 375). To arrest this heat buildup, in the controlled processing vase part, the laser power was reduced to 228 W (from 285 W) after layer 375 until the end of the build (layer 625). In Fig. 21, the thermal history trends for the vase parts were accurately captured by the graph theory approach with MAPE less than 2% and RMSE ranging from 4 °C to 6 °C. The graph theory simulation computation time is less than 3 min (161 s).

The spatial temperature distribution at select layers is mapped in Fig. 22. Compared to its fixed-processed counterpart, in the controlled-processed vase, decreasing the laser power to 228 W from the nominal 285 W from layer 375 onwards mitigated heat

buildup, particularly in the narrow neck region, and resulted in a smaller temperature gradient in the bulk part.

3.2.2. Part quality – Geometric integrity and feature resolution

While the difference in end-of-cycle surface temperatures between the fixed and controlled-processed vases shown in Fig. 21 are smaller compared to those between the cone-shaped parts (Fig. 16), the relatively complex shape of the vase produces a pronounced effect on the geometric integrity. In Fig. 23(a), it is evident visually, and subsequently affirmed on cross-sectioning the part parallel to the build direction, that the central cavity of the fixed-processed cone is sintered closed. This is because the elevated bulk part temperature, especially in the narrow neck region, during fixed processing (Fig. 22) fuses the powder trapped within the cavity. By contrast, as shown in Fig. 23(b) the central cavity for the controlled-processed vase is intact.

Further, in Fig. 23, dimensional analysis conducted from a nominal-to-actual comparison of the CAD model and from X-ray CT measurements revealed that the outer surface of the fixed-processed vase is larger than its nominal CAD model; the deviation exceeds +0.1 mm for the majority of the surface. The positive deviation, shown in a red hue on the figure, indicates that the part is larger than the CAD model. Also, in Fig. 23(a), partially fused satellite powder was adhered to the inner, as well as the outer, surfaces of the fixed-processed vase. By contrast, the vase produced under controlled processing maintains its geometric integrity (Fig. 23
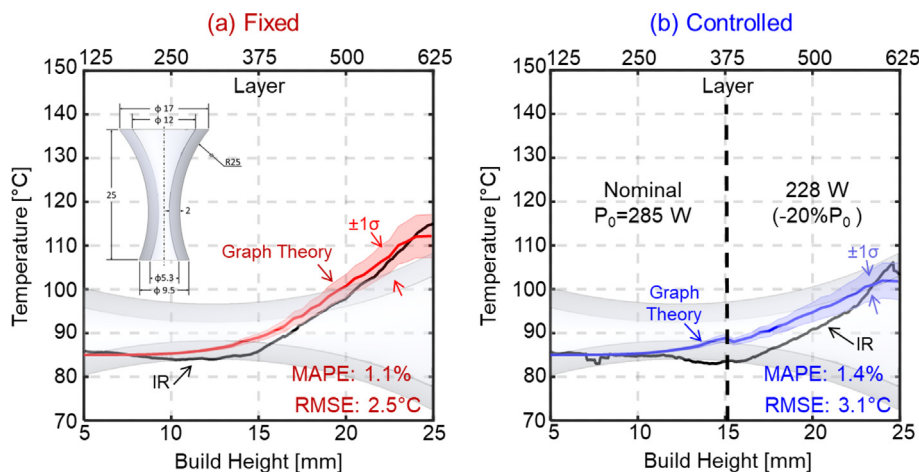
Fig. 21. Comparison of predicted and observed surface temperature for the vase-shaped parts. (a) fixed processing, and (b) controlled processing. The simulation was computed in less than 3 min with an error of less than 2%. The ± 1σ prediction interval is shown for both cases.
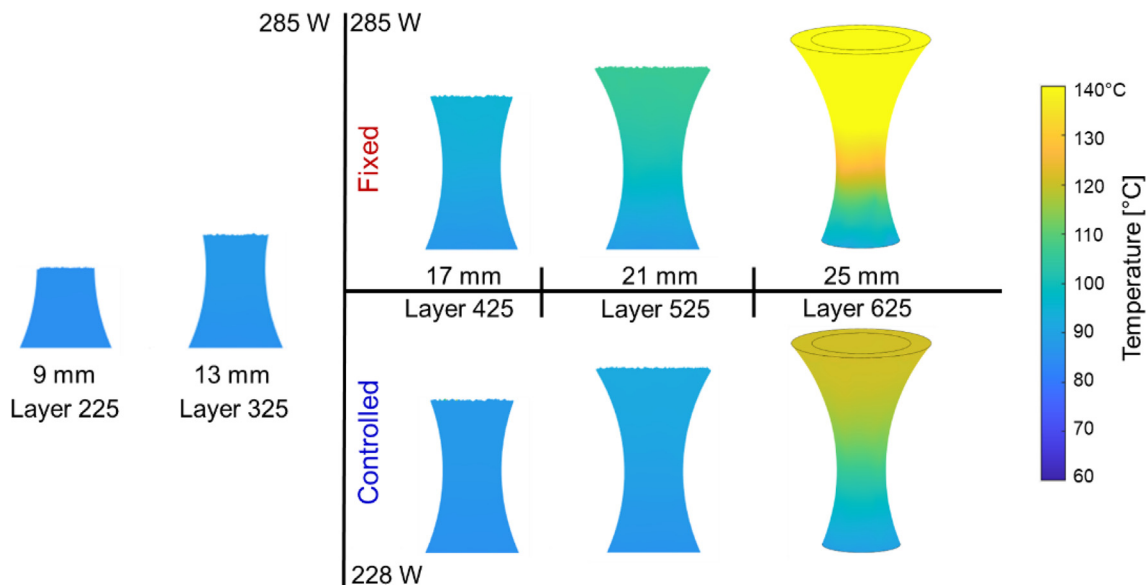
Fig. 22. Visualization of the temperature distribution in the vase parts predicted by the graph theory modeling approach for the fixed- and controlled-processed scenarios. In the controlled processing scenario, there is a distinctive reduction in the part temperature due to reduction of the laser power to 228 W after 15 mm (375 layers).
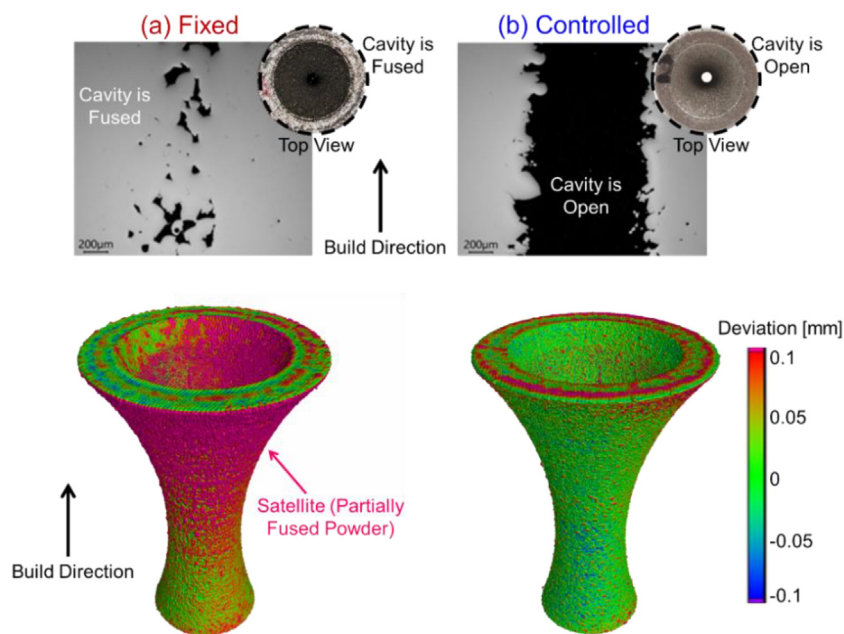

Fig. 23. (Top) Optical cross-section micrographs and (bottom) nominal-to-actual X-ray CT dimensional analysis of the vase-shaped parts. (a) In fixed processing the central cavity of the vase is fused and has satellite particles adhered to the internal and external surfaces on account of overheating. The nominal-to-actual dimensional computation to CAD (from X-ray CT analysis) reveals that the fixed-processed vase has a positive deviation larger than 0.1 mm consistent with over-melting of powder. (b) The controlled-processed cone has an intact cavity, negligible satellite powder is adhered to the surface, and there is minimal deviation from the design dimensions.

(b)) and is largely free of partially fused satellite particles adhered to the surface.

Comparison of the thermal history in Fig. 21 suggests there is less than a 15 °C difference in the end-of-cycle surface temperature between the fixed and controlled processing cases. By contrast, the corresponding difference for the cone was more than 50 °C (Fig. 16). Despite this relatively smaller difference in end-of-cycle surface temperature, the controlled processing sample has an intact cavity, while the cavity is blocked for the fixed processing case. As seen from the spatial temperature distribution map in Fig. 22, reducing the laser power in higher layers beyond 15 mm build height (layer 375) during controlled processing not only

decreased the surface temperature of the current layer, but also diminished the extent of reheating in preceding layers and the overall heat flux through the bulk part.

The increased temperature of the previous layers in fixed processing is evident in Fig. 24, where the thermal history is tracked at a specific location on the surface of the part at a build height of 13 mm (layer 325). Each peak in Fig. 24 corresponds to the melting of the subsequent layers above. The image shown in the inset of Fig. 24 is the predicted spatial temperature distribution at layer 325 when layer 425 is being deposited. In Fig. 24(a), the elevated bulk temperature of the fixed-processed vase melts the powder trapped in the cavity. Controlled processing (Fig. 24(b)) reduces
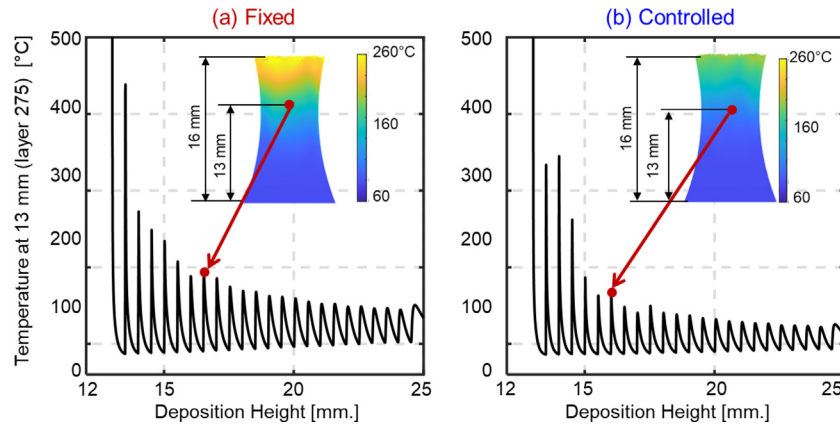
Fig. 24. Thermal history at a fixed location (13 mm, layer 325) for (a) fixed processing, and (b) controlled processing. Controlled processing reduced the temperature in previous layers compared to fixed processing thus mitigating melting of powder trapped in the cavity.

the bulk temperature, and consequently mitigates over-melting of powder particles within the cavity.

The foregoing observation underscores the importance of controlling the thermal history of not just the topmost layer, but also that of the bulk part. Such control of the bulk part temperature would not be feasible using purely reactive feedback process control mechanisms based on infrared thermal camera measurements of only the part end-of-cycle surface temperature.

3.3. Frame

3.3.1. Thermal history

The graph theory simulated thermal history prediction and the experimentally observed surface temperature trends for the frame parts are shown in Fig. 25. For the fixed processing condition (Fig. 25(a)), a rapid increase in surface temperature was observed towards the last 2 mm of the frame part (layers 575 to 625) during melting of the horizontal overhang section at the top. Heat buildup in the overhang region occurs due to the restricted thermal conduction pathway – the powder contained within the hollow frame acts as an insulator and impedes heat transfer to the build plate.

To counteract this sharp increase in temperature of the overhang region, in the controlled processing frame, the laser power is reduced to 228 W for the last 5 mm of processing (layer 500 to 625). The resulting thermal history derived from the graph theory simulation and observed from the infrared thermal camera are

shown in Fig. 25(b). Wherein the error between the simulated and observed thermal history is within 1.5% (MAPE) and the predictions were obtained in less than 10 min (557 s). The steep heat buildup toward the last 2 mm in the fixed-processed part is visually corroborated in the spatial thermal simulation snapshots shown in Fig. 26. As in previous cases, controlled processing reduces the bulk part temperature, and the spatial temperature gradient.

#### 3.3.2. Part quality – geometric integrity and microstructure evolution

The result of the controlled processing strategy on geometric integrity for the frame is shown in Fig. 27. The increased temperature in the fixed-processed part causes geometric inaccuracies and inferior surface finish. From the X-ray CT dimensional analysis of the fixed-processed frame in Fig. 27(a), the poor resolution of the overhang region is evident.

Further, satellite particles from partially melted powder are adhered to the inner and outer surfaces of the part. For the controlled processing condition, shown in Fig. 27(b), these geometry and surface flaws are reduced significantly.

Further, the wall thickness of the two frame parts was measured from the X-ray CT slices. As observed in Fig. 28, the mean wall thickness of the fixed-processed frame part is ∼ 1.68 mm, viz., 0.18 mm larger than the designed thickness of 1.5 mm. In contrast, the mean wall thickness for the controlled processing is ∼ 1.57 mm, i.e., a deviation of only 0.07 mm from the nominal.
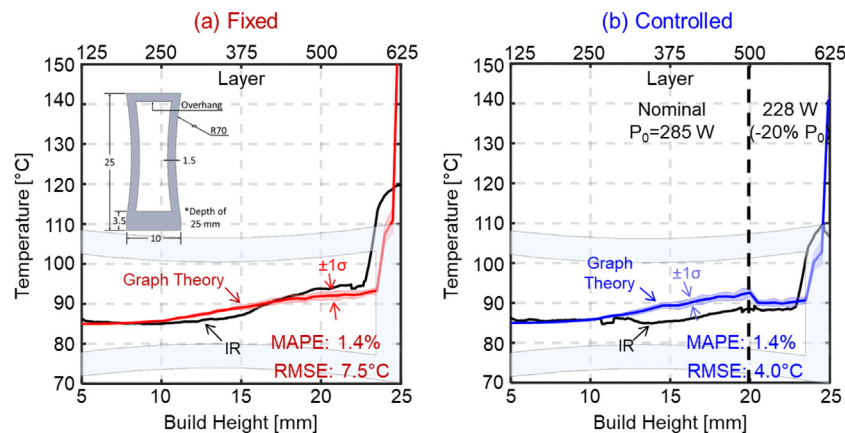

Fig. 25. Comparison of observed and predicted surface temperature trends for the frame shape (a) fixed processing and (b) controlled processing. The steep increase in temperature observed in the last 2 mm of build height near the top of the fixed-processing case in (a) is mitigated in the controlled processing case (b) by reducing the laser power to 228 W from the nominal 285 W. The simulation was calculated within 10 min with error less than 2% (MAPE). The ± 1σ prediction interval is shown for both cases.
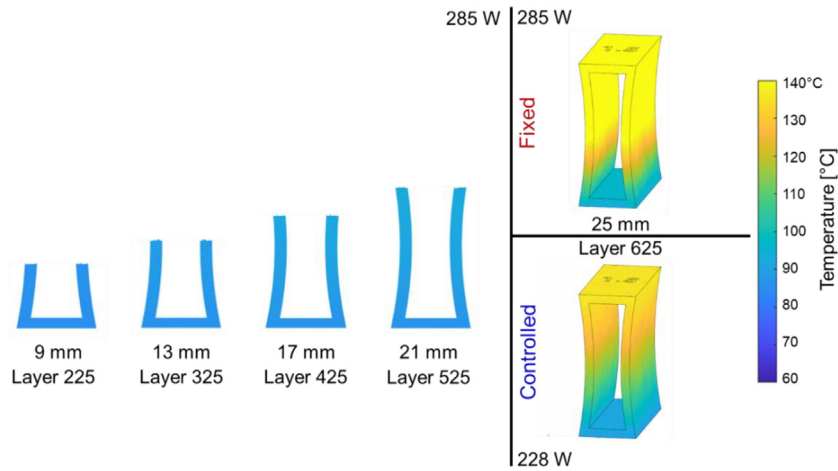
Fig. 26. Comparison of the temperature distribution between the fixed and controlled processing frame parts at select layers. The reduction of laser power to 228 W in the controlled processing sample beyond 20 mm build height (layer 500) mitigated heat buildup, and resulted in a smaller variation in the spatial temperature gradient.
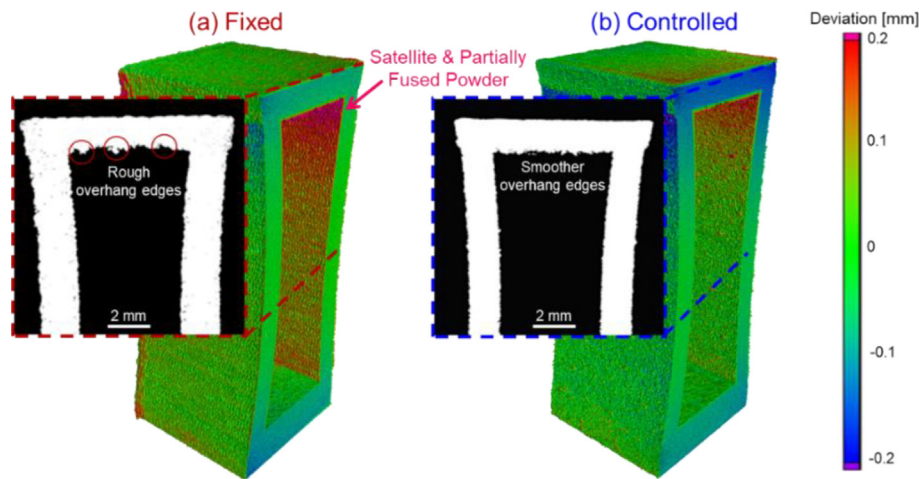
Fig. 27. X-ray CT nominal-to-actual comparison for (a) fixed and (b) controlled processing. In the case of fixed processing (a), the overhang region has satellite particle adhered to the part underside, and the external surfaces are symptomatic of heat buildup. These result in relatively degraded overall dimensional integrity and rougher surface finish on the underside of the overhang. In contrast, the controlled-processed frame (b) has improved surface finish and resolution in the overhang region.
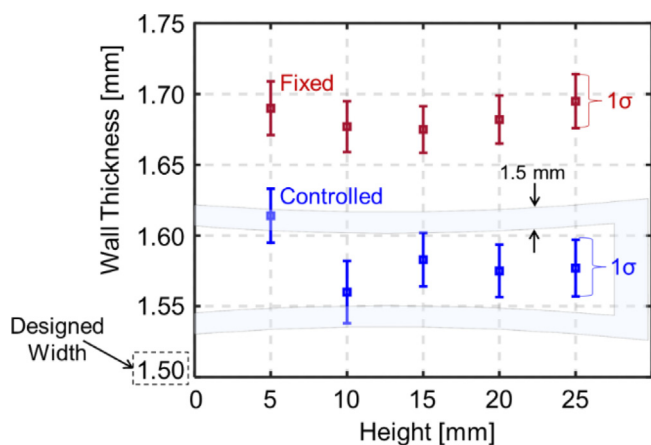
Fig. 28. Effect of fixed and controlled processing on the thickness (width) of the wall of the frame. The nominal designed wall width was 1.5 mm. The wall thickness for the controlled-processed sample was 1.57 mm, and 1.68 mm for the fixed processing case.

3.4. Bridge

3.4.1. Thermal history

The comparison of the predicted and observed thermal history for the fixed and controlled-processed bridge-shaped part are shown in Fig. 29(a) and (b) respectively. The temperature in the bridge part after 15 mm build height (layer 375) increases considerably due to the insulating properties of the un-melted powder beneath the overhang span regions.

In the case of the controlled-processed part, at layer 375 and beyond the steep increase in temperature is mitigated by reducing the laser power to 228 W (from 285 W). For example, at layer 500 (20 mm build height) the steady state end-of-cycle surface temperature for the fixed-processed bridge exceeds 120 °C (Fig. 29 (a)) compared to ∼ 100 °C (Fig. 29(b)) for the controlled-processed part. These surface temperature trends are accurately predicted by the graph theory approach (MAPE less than 3% and RMSE ∼ 7 °C). The simulation converged in just over 2 min.

The foregoing temporal thermal history trends are corroborated in the spatial temperature distribution plots in Fig. 30. A significant heat buildup in the bulk part is noted for the fixed processing scenario, particularly in the region of the overhang sections of the
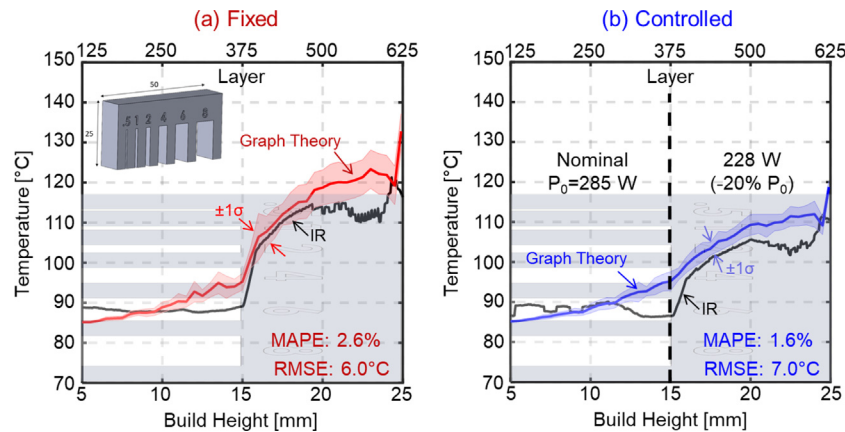
Fig. 29. Comparison of the model derived surface temperature trends and IR data for (a) fixed processing, and (b) controlled processing. Note the steep increase in thermal history in (a) beyond 15 mm (325 layers) due to un-melted powder in the gaps which act as a thermal insulator. This steep increase in surface temperature is mitigated by reducing the laser power to 228 W. The simulation converged in a little over 2 min (122 s) with error less than 2.5% (MAPE). The $\pm 1\sigma$ prediction interval is shown for both cases.
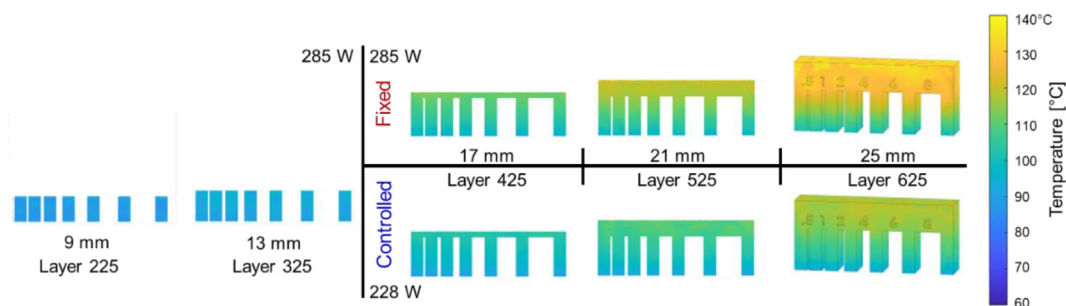
Fig. 30. Comparison of the thermal history for fixed and controlled processing for the bridge. The laser power is reduced to 228 W at layer 375 (15 mm) for the controlled processing condition, and consequently, the steep increase in temperature in the overhang span region is reduced.

bridge. Controlled processing substantially suppresses the heat buildup in the overhang span.

3.4.2. Part quality – geometric integrity and feature resolution

The differences in the temperature distribution of the bridge part produced under fixed and controlled processing, translate into prominent differences in geometric integrity. The gap between each of the six spans between the legs is assessed visually using optical microscopy.

Visual examination of the fixed and controlled-processed parts, as shown in Fig. 31, reveals that compared to controlled-processing, for the fixed processing condition, the finest 0.5 mm gap was smaller than designed and the resolution of the inset lettering is inferior. The reduction in the gap in the fixed-processed sample is due to over-melting of powder trapped underneath the span (similar to the vase and frame parts) on account of the elevated bulk part temperature.

4. Conclusions and future work

We developed and applied model-driven feedforward control to mitigate heat buildup and prevent subsequent flaw formation in parts made using the laser powder bed fusion (LPBF) additive manufacturing process. As opposed to printing the entire part at a constant parameter set, the key idea was to adjust two process parameters, namely, laser power and dwell time between layers, to mitigate heat buildup based on predictions from a computational thermal model.

The effectiveness of the process parameters optimized based on the feedforward control approach was demonstrated by printing two build plates, each consisting of Nickel Alloy 718 parts of 10 different types of geometries. Extensive post-process characterization was conducted on these parts to quantify their microstructure, microhardness, surface finish, and geometric integrity. It was observed that feedforward control produced parts with finer grain size, increased microhardness, improved geometric integrity and resolution, and reduced surface flaws.

From an industry vista, using this approach, practitioners can anticipate potential quality issues due to heat buildup in the part before it is printed, and accordingly modify (optimize) the processing parameters or part design. Such a proactive, physics-aided process parameter and design optimization approach can significantly reduce the need for expensive build-and-test experiments, and thus accelerate the time-to-market of additively manufactured parts.

In our future research, the feedforward approach will be automated so that potential regions of heat buildup are identified and corrected autonomously during the process planning stage through purpose-built algorithms. Further, instead of the broad strategy of reducing heat buildup across layers, forthcoming research will focus on controlling specific process outcomes, such as residual stresses and microstructure heterogeneity.

Data availability

Data will be made available on request.
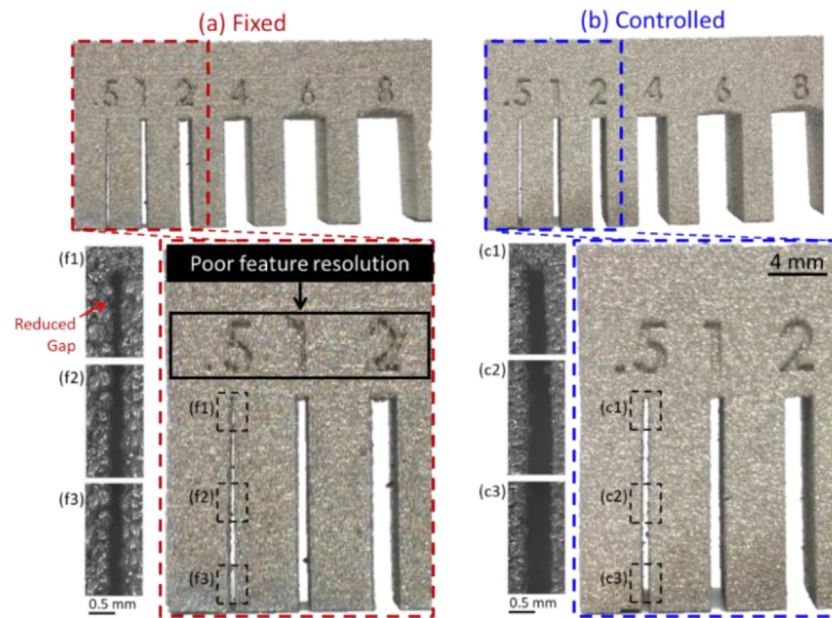
Fig. 31. Comparison of the geometric resolution of (a) fixed and (b) controlled-processed bridge part. The geometric resolution of the controlled processing bridges is superior in terms the gap between the legs as well as the engraved numbering.

Declaration of Competing Interest

The authors declare that they have no known competing financial interests or personal relationships that could have appeared to influence the work reported in this paper.

Acknowledgements

References

[1] L. Ladani, M. Sadeghilaridjani, Review of Powder Bed Fusion Additive Manufacturing for Metals, Metals 11 (2021), https://doi.org/10.3390/met11091391.

[2] T. DebRoy, H.L. Wei, J.S. Zuback, T. Mukherjee, J.W. Elmer, J.O. Milewski, A.M. Beese, A. Wilson-Heid, A. De, W. Zhang, Additive manufacturing of metallic components – Process, structure and properties, Prog. Mater. Sci. 92 (2018) 112–224, https://doi.org/10.1016/j.pmatsci.2017.10.001.

[3] A. Mostafaei, C. Zhao, Y. He, S. Reza Ghiaasiaan, B. Shi, S. Shao, N. Shamsaei, Z. Wu, N. Kouraytem, T. Sun, J. Pauza, J.V. Gordon, B. Webler, N.D. Parab, M. Asherloo, Q. Guo, L. Chen, A.D. Rollett, Defects and anomalies in powder bed fusion metal additive manufacturing, Curr. Opin. Solid State Mater. Sci. 26 (2022), https://doi.org/10.1016/j.cossms.2021.100974 100974.

[4] Z. Snow, A.R. Nassar, E.W. Reutzel, Invited Review Article: Review of the formation and impact of flaws in powder bed fusion additive manufacturing, Addit. Manuf. 36 (2020), https://doi.org/10.1016/j.addma.2020.101457 101457.

[5] L. Dowling, J. Kennedy, S. O'Shaughnessy, D. Trimble, A review of critical repeatability and reproducibility issues in powder bed fusion, Mater. Des. 186 (2020), https://doi.org/10.1016/j.matdes.2019.108346 108346.

[6] J.P. Oliveira, A.D. LaLonde, J. Ma, Processing parameters in laser powder bed fusion metal additive manufacturing, Mater. Des. 193 (2020), https://doi.org/10.1016/j.matdes.2020.108762 108762.

[7] W.J. Sames, F.A. List, S. Pannala, R.R. Dehoff, S.S. Babu, The metallurgy and processing science of metal additive manufacturing, Int. Mater. Rev. 61 (2016) 315–360, https://doi.org/10.1080/09506608.2015.1116649.

[8] R.J. Williams, A. Piglione, T. Rønneberg, C. Jones, M.-S. Pham, C.M. Davies, P.A. Hooper, In situ thermography for laser powder bed fusion: Effects of layer temperature on porosity, microstructure and mechanical properties, Addit. Manuf. 30 (2019), https://doi.org/10.1016/j.addma.2019.100880 100880.

[9] R. Yavari, Z. Smoqi, A. Riensche, B. Bevans, H. Kobir, H. Mendoza, H. Song, K. Cole, P. Rao, Part-scale thermal simulation of laser powder bed fusion using graph theory: Effect of thermal history on porosity, microstructure evolution, and recoater crash, Mater. Des. 204 (2021), https://doi.org/10.1016/j.matdes.2021.109685 109685.

[10] S. Li, J. Yang, Z. Wang, Multi-laser powder bed fusion of Ti-6.5Al-2Zr-Mo-V alloy powder: Defect formation mechanism and microstructural evolution,

Powder Technol. 384 (2021) 100–111, https://doi.org/10.1016/j.powtec.2021.02.010.

[11] N.H. Paulson, B. Gould, S.J. Wolff, M. Stan, A.C. Greco, Correlations between thermal history and keyhole porosity in laser powder bed fusion, Addit. Manuf. 34 (2020), https://doi.org/10.1016/j.addma.2020.101213 101213.

[12] H.L. Wei, T. Mukherjee, W. Zhang, J.S. Zuback, G.L. Knapp, A. De, T. DebRoy, Mechanistic models for additive manufacturing of metallic components, Prog. Mater Sci. 116 (2021), https://doi.org/10.1016/j.pmatsci.2020.100703 100703.

[13] F. Imani, A. Gaikwad, M. Montazeri, P. Rao, H. Yang, E. Reutzel, Process mapping and in-process monitoring of porosity in laser [owder bed fusion using layerwise optical imaging, J. Manuf. Sci. Eng. 140 (2018), https://doi.org/10.1115/1.4040615.

[14] N. Sanaei, A. Fatemi, N. Phan, Defect characteristics and analysis of their variability in metal L-PBF additive manufacturing, Mater. Des. 182 (2019), https://doi.org/10.1016/j.matdes.2019.108091 108091.

[15] M. Seifi, A. Salem, J. Beuth, O. Harrysson, J.J. Lewandowski, Overview of materials qualification needs for metal additive manufacturing, JOM 68 (2016) 747–764, https://doi.org/10.1007/s11837-015-1810-0.

[16] A. Pfaff, M. Jäcklein, M. Schlager, W. Harwick, K. Hoschke, F. Balle, An empirical approach for the development of process parameters for laser powder bed fusion, Materials 13 (2020), https://doi.org/10.3390/ma13235400.

[17] N. Ahmed, I. Barsoum, G. Haidemenopoulos, R.K.A. Al-Rub, Process parameter selection and optimization of laser powder bed fusion for 316L stainless steel: A review, J. Manuf. Processes 75 (2022) 415–434, https://doi.org/10.1016/j.jmapro.2021.12.064.

[18] R. Seede, D. Shoukr, B. Zhang, A. Whitt, S. Gibbons, P. Flater, A. Elwany, R. Arroyave, I. Karaman, An ultra-high strength martensitic steel fabricated using selective laser melting additive manufacturing: Densification, microstructure, and mechanical properties, Acta Mater. 186 (2020) 199–214, https://doi.org/10.1016/j.actamat.2019.12.037.

[19] O. Diegel, A. Nordin, D. Motte, A Pracitcal Guide to Design for Additive Manufacturing, Springer Nature Singapore Pte Ltd., in, 2019, pp. 978–981.

[20] N. Kouraytem, X. Li, W. Tan, B. Kappes, A.D. Spear, Modeling process–structure–property relationships in metal additive manufacturing: a review on physics-driven versus data-driven approaches, Jo. Phys.: Mater. 4 (2021) 32002, https://doi.org/10.1088/2515-7639/abca7b.

[21] Y. Huang, M.C. Leu, J. Mazumder, A. Donmez, Additive Manufacturing: Current state, future potential, gaps and needs, and recommendations, J. Manuf. Sci. Eng. 137 (2015), https://doi.org/10.1115/1.4028725.

[22] A. Polonsky, T. Pollock, Closing the science gap in 3D metal printing, Science 368 (2020) 583–584, https://doi.org/10.1126/science.abb4938.

[23] R. Yavari, R. Williams, A. Riensche, P.A. Hooper, K.D. Cole, L. Jacquemetton, H. (Scott) Halliday, P.K. Rao, Thermal modeling in metal additive manufacturing using graph theory – Application to laser powder bed fusion of a large volume impeller, Additive Manufacturing. 41 (2021) 101956. 10.1016/j.addma.2021.101956.

[24] K.D. Cole, A. Riensche, P.K. Rao, Discrete Green's functions and spectral graph theory for computationally efficient thermal modeling, Int. J. Heat Mass Transf. 183 (2022), https://doi.org/10.1016/j.ijheatmasstransfer.2021.122112 122112.

[25] M.H. Kobir, R. Yavari, A.R. Riensche, B.D. Bevans, L. Castro, K.D. Cole, P. Rao, Prediction of recoater crash in laser powder bed fusion additive manufacturing using graph theory thermomechanical modeling, Prog. Addit. Manuf. (2022), https://doi.org/10.1007/s40964-022-00331-5.

[26] M. Reza Yavari, R.J. Williams, K.D. Cole, P.A. Hooper, P. Rao, Thermal Modeling in Metal Additive Manufacturing Using Graph Theory: Experimental validation with laser powder bed fusion using in situ infrared thermography data, J. Manuf. Sci. Eng. 142 (2020), https://doi.org/10.1115/1.4047619.

[27] M.R. Yavari, K.D. Cole, P. Rao, Thermal modeling in metal additive manufacturing using graph theory, J. Manuf. Sci. Eng. 141 (2019), https://doi.org/10.1115/1.4043648.

[28] K.D. Cole, M.R. Yavari, P.K. Rao, Computational heat transfer with spectral graph theory: Quantitative verification, Int. J. Therm. Sci. 153 (2020), https://doi.org/10.1016/J.IJTHERMALSCI.2020.106383 106383.

[29] Q. Zhong, X. Tian, X. Huang, C. Huo, D. Li, Using feedback control of thermal history to improve quality consistency of parts fabricated via large-scale powder bed fusion, Addit. Manuf. 42 (2021), https://doi.org/10.1016/j.addma.2021.101986 101986.

[30] G. Tapia, A. Elwany, A review on process monitoring and control in metal-based additive manufacturing, J. Manuf. Sci. Eng. 136 (2014), https://doi.org/10.1115/1.4028540.

[31] M. Mani, B.M. Lane, M.A. Donmez, S.C. Feng, S.P. Moylan, A review on measurement science needs for real-time control of additive manufacturing metal powder bed fusion processes, Int. J. Prod. Res. 55 (2017) 1400–1418, https://doi.org/10.1080/00207543.2016.1223378.

[32] R. McCann, M.A. Obeidi, C. Hughes, É. McCarthy, D.S. Egan, R.K. Vijayaraghavan, A.M. Joshi, V. Acinas Garzon, D.P. Dowling, P.J. McNally, D. Brabazon, In-situ sensing, process monitoring and machine control in Laser Powder Bed Fusion: A review, Addit. Manuf. 45 (2021), https://doi.org/10.1016/j.addma.2021.102058 102058.

[33] M. Vlasea, B. Lane, F. Lopez, S. Mekhontsev, M. Donmez, Development of powder bed fusion additive manufacturing test bed for enhanced real time process control, in: Solid Freeform Fabrication Symposium, Austin, TX, 2015. https://tsapps.nist.gov/publication/get_pdf.cfm?pub_id=919042.

[34] M. Grasso, B.M. Colosimo, Process defects and in situ monitoring methods in metal powder bed fusion: a review, Meas. Sci. Technol. 28 (2017) 44005, https://doi.org/10.1088/1361-6501/aa5c4f.

[35] M. Grasso, A. Remani, A. Dickins, B.M. Colosimo, R.K. Leach, In-situ measurement and monitoring methods for metal powder bed fusion: an updated review, Meas. Sci. Technol. 32 (2021), https://doi.org/10.1088/1361-6501/ac0b6b 112001.

[36] Y. Ren, Q. Wang, Gaussian-process based modeling and optimal control of melt-pool geometry in laser powder bed fusion, J. Intell. Manuf. (2021), https://doi.org/10.1007/s10845-021-01781-4.

[37] V. Renken, L. Lübbert, H. Blom, A. von Freyberg, A. Fischer, Model assisted closed-loop control strategy for selective laser melting, Procedia CIRP 74 (2018) 659–663, https://doi.org/10.1016/j.procir.2018.08.053.

[38] E. Vasileska, A.G. Demir, B.M. Colosimo, B. Previtali, A novel paradigm for feedback control in LPBF: layer-wise correction for overhang structures, Adv. Manuf. 10 (2022) 326–344, https://doi.org/10.1007/s40436-021-00379-6.

[39] A. Shkoruta, B. Park, S. Mishra, An empirical model for feedforward control of laser powder bed fusion, (2022). 10.48550/ARXIV.2201.09978.

[40] H. Yeung, B. Lane, J. Fox, Part geometry and conduction-based laser power control for powder bed fusion additive manufacturing, Addit. Manuf. 30 (2019), https://doi.org/10.1016/j.addma.2019.100844 100844.

[41] H. Yeung, B. Lane, A residual heat compensation based scan strategy for powder bed fusion additive manufacturing, Manuf. Lett. 25 (2020) 56–59, https://doi.org/10.1016/j.mfglet.2020.07.005.

[42] A. Papacharalampopoulos, P. Stavropoulos, J. Stavridis, Adaptive Control of Thermal Processes: Laser welding and additive manufacturing paradigms, Procedia CIRP 67 (2018) 233–237, https://doi.org/10.1016/j.procir.2017.12.205.

[43] Q. Wang, P. (Pan) Michaleris, A.R. Nassar, J.E. Irwin, Y. Ren, C.B. Stutzman, Model-based feedforward control of laser powder bed fusion additive manufacturing, Additive Manuf. 31 (2020) 100985. 10.1016/j.addma.2019.100985.

[44] C.L. Druzgalski, A. Ashby, G. Guss, W.E. King, T.T. Roehling, M.J. Matthews, Process optimization of complex geometries using feed forward control for laser powder bed fusion additive manufacturing, Addit. Manuf. 34 (2020), https://doi.org/10.1016/j.addma.2020.101169 101169.

[45] F. Ogoke, A.B. Farimani, Thermal control of laser powder bed fusion using deep reinforcement learning, Addit. Manuf. 46 (2021), https://doi.org/10.1016/j.addma.2021.102033 102033.

[46] K.S. Ramani, C. He, Y.-L. Tsai, C.E. Okwudire, SmartScan: An intelligent scanning approach for uniform thermal distribution, reduced residual stresses and deformations in PBF additive manufacturing, Addit. Manuf. 52 (2022), https://doi.org/10.1016/j.addma.2022.102643 102643.

[47] J. Lee, V. Prabhu, Simulation modeling for optimal control of additive manufacturing processes, Addit. Manuf. 12 (2016) 197–203, https://doi.org/10.1016/j.addma.2016.05.002.

[48] T.T. Roehling, S.S.Q. Wu, S.A. Khairallah, J.D. Roehling, S.S. Soezeri, M.F. Crumb, M.J. Matthews, Modulating laser intensity profile ellipticity for microstructural control during metal additive manufacturing, Acta Mater. 128 (2017) 197–206, https://doi.org/10.1016/j.actamat.2017.02.025.

[49] Z. Luo, Y. Zhao, A survey of finite element analysis of temperature and thermal stress fields in powder bed fusion Additive Manufacturing, Addit. Manuf. 21 (2018) 318–332, https://doi.org/10.1016/j.addma.2018.03.022.

[50] M. Gouge, P. Michaleris, E. Denlinger, J. Irwin, Chapter 2 - The Finite Element Method for the Thermo-Mechanical Modeling of Additive Manufacturing Processes, in: Thermo-Mechanical Modeling of Additive Manufacturing, Butterworth-Heinemann, 2018, pp. 19–38. 10.1016/B978-0-12-811820-7.00003-3.

[51] N. Peter, Z. Pitts, S. Thompson, A. Saharan, Benchmarking build simulation software for laser powder bed fusion of metals, Addit. Manuf. 36 (2020), https://doi.org/10.1016/j.addma.2020.101531 101531.

[52] Q. Wang, P. Michaleris, M. Pantano, C. Li, Y. Ren, A.R. Nassar, Part-scale thermal evolution and post-process distortion of Inconel-718 builds fabricated by laser powder bed fusion, J. Manuf. Processes 81 (2022) 865–880, https://doi.org/10.1016/j.jmapro.2022.07.026.

[53] S. Sanchez, P. Smith, Z. Xu, G. Gaspard, C.J. Hyde, W.W. Wits, I.A. Ashcroft, H. Chen, A.T. Clare, Powder Bed Fusion of nickel-based superalloys: A review, Int. J. Mach. Tools Manuf 165 (2021), https://doi.org/10.1016/j.ijmachtools.2021.103729 103729.

[54] G. Mohr, S.J. Altenburg, K. Hilgenberg, Effects of inter layer time and build height on resulting properties of 316L stainless steel processed by laser powder bed fusion, Addit. Manuf. 32 (2020), https://doi.org/10.1016/j.addma.2020.101080 101080.

[55] Z. Smoqi, A. Gaikwad, B. Bevans, M.H. Kobir, J. Craig, A. Abul-Haj, A. Peralta, P. Rao, Monitoring and prediction of porosity in laser powder bed fusion using physics-informed meltpool signatures and machine learning, J. Mater. Process. Technol. 304 (2022), https://doi.org/10.1016/j.jmatprotec.2022.117550 117550.

[56] B. Lane, S. Moylan, E.P. Whitenton, L. Ma, Thermographic measurements of the commercial laser powder bed fusion process at NIST, Rapid Prototyping J. 22 (2016) 778–787, https://doi.org/10.1108/RPJ-11-2015-0161.

[57] S. Moylan, E. Whitenton, B. Lane, J. Slotwinski, Infrared thermography for laser-based powder bed fusion additive manufacturing processes, AIP Conf. Proc. 1581 (2014) 1191–1196, https://doi.org/10.1063/1.4864956.

[58] E. Rodriguez, J. Mireles, C.A. Terrazas, D. Espalin, M.A. Perez, R.B. Wicker, Approximation of absolute surface temperature measurements of powder bed

fusion additive manufacturing technology using in situ infrared thermography, Addit. Manuf. 5 (2015) 31–39, https://doi.org/10.1016/j.addma.2014.12.001.

[59] B. Schoinochoritis, D. Chantzis, K. Salonitis, Simulation of metallic powder bed additive manufacturing processes with the finite element method: A critical review, Proceedings of the Institution of Mechanical Engineers, Part B: Journal of Engineering Manufacture. 231 (2015) 96–117. 10.1177/0954405414567522.

[60] S.M. Yusuf, N. Gao, Influence of energy density on metallurgy and properties in metal additive manufacturing, Mater. Sci. Technol. 33 (2017) 1269–1289, https://doi.org/10.1080/02670836.2017.1289444.

[61] U. Scipioni Bertoli, A.J. Wolfer, M.J. Matthews, J.-P.-R. Delplanque, J.M. Schoenung, On the limitations of Volumetric Energy Density as a design parameter for Selective Laser Melting, Mater. Des. 113 (2017) 331–340, https://doi.org/10.1016/j.matdes.2016.10.037.

[62] A. Riensche, J. Severson, R. Yavari, N.L. Piercy, K.D. Cole, P. Rao, Thermal modeling of directed energy deposition additive manufacturing using graph theory, Rapid Prototyping Journal. ahead-of-p (2022). 10.1108/RPJ-07-2021-0184.

[63] A. Gaikwad, B. Giera, G.M. Guss, J.-B. Forien, M.J. Matthews, P. Rao, Heterogeneous sensing and scientific machine learning for quality assurance in laser powder bed fusion – A single-track study, Addit. Manuf. 36 (2020), https://doi.org/10.1016/j.addma.2020.101659 101659.

[64] S. Katayama, A. Matsunawa, Solidification microstructure of laser welded stainless steels, Int. Congr. Appl. Lasers Electro-Optics 1984 (1984) 60–67, https://doi.org/10.2351/1.5057623.

[65] K.H.W. Seah, J. Hemanth, S.C. Sharma, Effect of the cooling rate on the dendrite arm spacing and the ultimate tensile strength of cast iron, J. Mater. Sci. 33 (1998) 23–28, https://doi.org/10.1023/A:1004321007806.